Hot spot formation induced by RF heating in tokamak plasmas

王, 雲飛

出版情報：Kyushu University, 2023, 博士（理学）, 課程博士
バージョン：
権利関係：

Hot spot formation induced by RF heating in tokamak plasmas

（トカマクプラズマにおける高周波加熱によるホット・スポット形成）

Doctoral Thesis

July 2023

By

WANG YUNFEI　（王　雲飛）

Supervisor: Prof. HANADA KAZUAKI　（花田　和明）

Advanced Energy Engineering Science

Interdisciplinary Graduate School of Engineering Sciences

Kyushu University

ABSTRACT

Magnetic confinement fusion research is entering a new era, with increasing attention being paid to high-parameter long-pulse plasma operation with high injection power, in order to meet the operation requirements of future fusion power plants. The study of power balance plays an important role in achieving the desired objectives, and the breaking of power balance is one of the significant reasons for the long-pulse discharge termination. Hot spot is one of the manifestations of excessive local heat load on plasma facing components (PFCs) and can interact strongly with PFCs materials, leading to impurity sputtering. The transport of impurities into the main plasma will break the power balance and cause the discharge termination. Additionally, hot spot can cause melting of the PFCs materials, which will threaten the safe operation of the device. Therefore, the study of the formation mechanisms of hot spot is critical for the safe operation of both present and future fusion devices. Hot spots have been observed during radiofrequency (RF) wave injection on many devices, and the mechanisms of their formation have been investigated. The hot spot in Q-shu University Experiments with Steady-State Spherical Tokamak (QUEST) was caused by the poloidal orbit deviation of the energetic electrons accelerated by electron cyclotron wave (ECW).

In this thesis, a new relativistic guiding center orbit code (RGCO) was thus developed as a powerful tool to explore relevant physics topics. The hot spot on the lower divertor in Experimental Advanced Superconducting Tokamak (EAST) has been observed when lower hybrid wave (LHW) injection. This thesis systematically studies the formation mechanism and energy source of hot spots in EAST by the combination of experiment data and code simulations. It is found that the scrape-off layer (SOL) magnetic topology plays an important role in the hot spot formation, and the energy deposition in the SOL through LHW collision damping is one of the important energy sources of hot spot formation. Notably, these findings provide a solution for hot spot mitigation, contributing to the achievement of 101.2 s long-pulse H-mode discharge in

EAST. This research will also help to accumulate experience for the safe plasma operation of future fusion power plants under long duration and high performance.

This thesis consists of the following chapters:

In Chapter 1, the background of this thesis is presented. The study of hot spot formation induced by RF heating in EAST and other magnetic confinement plasma devices is of great importance because hot spot formation on the PFCs could lead to the break of power balance during plasma operation, and to the termination of long-pulse discharges, which is not beneficial to the achievement of fusion goals. To better conduct this study, the magnetic confinement principle and magnetic configuration of the tokamak plasma are introduced. Additionally, a summary review of hot spot study in other devices is presented, as a cornerstone of this doctoral research.

In Chapter 2, the relativistic guiding center orbit code (RGCO) is introduced, with ripple magnetic field as a perturbation magnetic field also incorporated into the program. The actual geometry of PFCs in the device was also taken into consideration in the program, allowing for realistic electron orbit simulations for the study of energetic electron confinement and loss. Based on experimental data, the energetic electron orbit simulations conducted by RGCO reveal the fact that, the energetic electrons can be confined both inside and outside of the last closed flux surface (LCFS). Notably, at the outside of the LCFS and within a certain range of pitch angles, the electrons will move along the magnetic field lines (MFLs) and reach directly to the upper and lower divertors. These parts of energetic electrons may contribute to the hot spot formation in QUEST.

In Chapter 3, the main diagnostics systems used for measuring the heat load on PFCs of EAST are introduced. The heat load distribution between different PFCs during EAST discharges was analyzed through the calorimetric measurement, and the water-cooling performance of the main PFCs in EAST was evaluated. The results demonstrate that these PFCs exhibit excellent water-cooling capacity and are suitable for future plasma operation in EAST with higher parameter and longer duration.

In Chapter 4, the impact of magnetic configuration in the SOL on the hot spot formation is researched. The reason of hot spot formation on the lower divertor of EAST during upper single null (USN) discharges is investigated, and it is found that the slight change of the SOL magnetic configuration can cause hot spot formation. This phenomenon is further explained intuitively through the MFLs tracking in the SOL. Meanwhile, combined with calorimetric measurement, it is discovered that the hot spot formation on the lower divertor is accompanied by a great variations of energy load distribution among different plasma facing components. These findings are confirmed in subsequent 101.2 s long-pulse H-mode discharge.

In Chapter 5, the experiment about two-frequency power modulation of the LHW has been performed and detailed researched in order to explore the energy source of the hot spot on the lower divertor of EAST. This experiment revealed the hot spot generation during low frequency LHW injection and mitigation during high frequency LHW injection. Theoretical analysis combined with simulation based on ray-tracing/Fokker–Planck model elucidated that LHW can transfer wave energy to electrons through collision damping in the SOL, and these electrons can move along open magnetic field lines in the SOL, then bombard the PFCs and cause hot spot generation. Lower frequency LHW tends to deposit more energy through collision damping compared to higher frequency LHW. This result agreed with the experimental observation in EAST.

In Chapter 6, an overall summary and a discussion of the future work are described.

TABLE OF CONTENTS

CHAPTER 1. Introduction

1.1 Nuclear fusion as a promising future energy source

Energy has been the driving force behind the development of human society.

With the development of human society, the demand for energy has been increasing. However, the large-scale exploitation of various non-renewable energy sources such as coal, oil, and natural gas has led to their depletion, causing humanity to face an energy crisis. In order to cope with the crisis, scientists have been exploring for solutions tirelessly. Various new energy sources have been discovered, such as solar energy, ocean energy, geothermal energy, wind energy, and so on. But all of them have not been widely applied due to their unstable supply and low energy conversion efficiency.

Eventually, scientists turned their attention to nuclear energy. According to Einstein's mass-energy equation $E = mc^2$, with the loss of mass in atomic nuclei, tremendous energy is released during the nuclear reaction. Nuclear reaction can be divided into nuclear fission reaction and nuclear fusion reaction. The first one to be peacefully utilized by humans is nuclear fission energy, huge amounts of fission energy are released when heavy atomic nuclei (mainly uranium or plutonium nuclei) split into two or more smaller atomic nuclei. Chicago Pile-1 (CP-1) [1] is widely recognized as the world's first artificial nuclear reactor. It achieved the first self-sustaining nuclear chain reaction on December 2, 1942, marking a major milestone in the validation of the chain nuclear fission theory. Building on this success, the Obninsk Nuclear Power Plant [2] in the Soviet Union commenced commercial operation on June 27, 1954, as the world's first nuclear power station to supply electricity to a power grid. There are now over 400 nuclear power plants worldwide, which has greatly alleviated the energy crisis of mankind. However, nuclear fission energy has three fatal flaws. The first is the depletion of the resource. The nuclear fission material uranium-235 is extracted from uranium ore, and its reserves on Earth are limited, which cannot meet the long-term use of humanity. The second is the disposal of radioactive nuclear waste from fission power plants, which has always plagued humanity. The third is the lack of safety. There have been many serious nuclear accidents at nuclear fission power plants in history, such as the Chernobyl disaster in Ukraine in 1986 and the Fukushima nuclear disaster in Japan in 2011. Nuclear accidents have caused significant adverse impacts on both humans and the environment, resulting in incalculable losses. The areas where these accidents occurred remain uninhabitable for humans.

The three disadvantages of nuclear fission energy are precisely the advantages of nuclear fusion energy. Nuclear fusion reactions release enormous energy when light atomic nuclei combine into heavier ones. The reaction between deuterium and tritium (D-T) is the easiest fusion reaction to achieve on Earth. Both deuterium and tritium can be obtained directly or indirectly from seawater, and their reserves are abundant. The reaction product of D-T fusion is helium gas, which already exists on Earth and is pollution-free. The strict conditions required for fusion reactions provide inherent safety for the operation of device. Therefore, the successful utilization of fusion energy will be the ultimate solution to the energy crisis of mankind.

There are three confinement methods for implementing nuclear fusion reactions: gravitational confinement [3], inertial confinement [4], and magnetic confinement [5]. The sun has been continuously producing light and heat for billions of years. These energies come from nuclear fusion reactions with gravitational confinement, which are enabled by the strong gravitational field generated by the huge mass of sun. Laser fusion is the most promising method among inertial confinement fusion techniques. The fundamental principle of laser fusion is to use an intensely powerful laser beam to uniformly irradiate a fuel target consisting of a mixture of deuterium and tritium, rapidly heating and compressing the target to a plasma state with high temperature and high density. Due to inertia, the scattering of the target pellet needs to take a certain amount of time, within this extremely short time, the nuclear fusion reaction can be quickly realized. On December 5, 2022, at the National Ignition Facility of Lawrence Livermore National Laboratory, scientist achieved a record-breaking fusion energy output of 3.15 MJ by delivering 2.05 MJ of energy to the target of deuterium and tritium [6, 7]. This marks the first time that a $Q > 1$ (Q, thermonuclear power produced divided by heating power supplied) result has been obtained using the D-T reaction.

Magnetic confinement fusion is a technique that uses a special configuration of magnetic fields to confine fusion fuel in the plasma state to a finite volume, allowing the fuel to undergo a controlled reaction and to release energy. Scientists have proposed various experiment devices with different magnetic configuration for magnetic confinement fusion, including magnetic mirrors [8, 9], stellarators [10-12], tokamaks [13-15] and so on. And the tokamak device is currently one of the most promising approaches to make significant progress toward commercialization of fusion power.

1.2 Plasma confinement in a tokamak

The concept of the tokamak device was proposed by Soviet scientists in the 1950s. It is a toroidal plasma confinement system in which the plasma is constrained by the magnetic field. The main magnetic field is the toroidal field generated by toroidal field coils, as shown in figure 1.1. To confine the plasma, a poloidal magnetic field is also required, which is produced mainly by plasma current itself, which moves in the toroidal direction. In addition, the poloidal magnetic field generated by poloidal field coils controls the shape and equilibrium of the plasma cross-section [14].

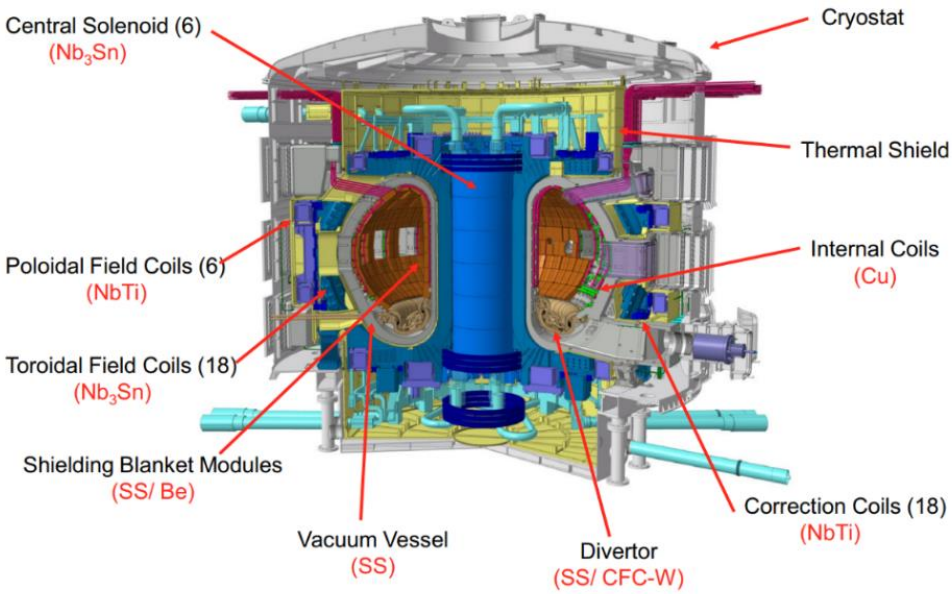

Figure 1.1. Schematic layout of the International Thermonuclear Experimental Reactor (ITER). (From http://www.iter.org)

The steps for plasma operation in a tokamak are as follows [14]: Firstly, pump in the vacuum chamber to make the air pressure close to vacuum, then puff the fuel gas into the vacuum chamber before the discharge. Secondly, improve the toroidal magnetic field to the predetermined value, charge the ohmic transformer to induce a toroidal electric field that ionizes the fuel gas and generates plasma. Thirdly, construct the required magnetic configuration by combining the poloidal magnetic field generated from the poloidal field coils and plasma current. Fourthly, further heat the plasma by a variety of auxiliary heating methods, to achieve the desired plasma parameters and operation state.

In which, the pre-ionization of the fuel gas can also be achieved using radiofrequency (RF) waves [16, 17]. The auxiliary heating methods mainly include energetic neutral beam injection (NBI) [18, 19] and RF wave injection. According to the wave frequency, there are three main types of RF heating, namely ion cyclotron resonant frequency (ICRF) heating [20], electron cyclotron resonance heating (ECRH) [21, 22] and lower hybrid wave (LHW) heating [23, 24]. The diagnostics system [25, 26] is an essential component of the tokamak and is used to measure the plasma parameters and confinement performance, such as density and temperature distributions of electron and ion, plasma current distribution, and impurity distribution. The diagnostics system is the experimental foundation for tokamak physics research and provides strong support for improving and developing tokamak operation. By integrating plasma diagnostics system, auxiliary heating system, coil system, and fuel supply system, the plasma control system (PCS) [27] can provide real-time feedback control of the plasma operation to achieve the desired plasma performance.

For simplicity, a tokamak can be considered as a toroidal symmetric system. The magnetic topology in the tokamak can be ideally considered as consisting of layers of nested magnetic surfaces, and the magnetic field lines lie in the magnetic surfaces [14], as shown in figure 1.2. The innermost magnetic surface degenerates into a line, namely the magnetic axis.

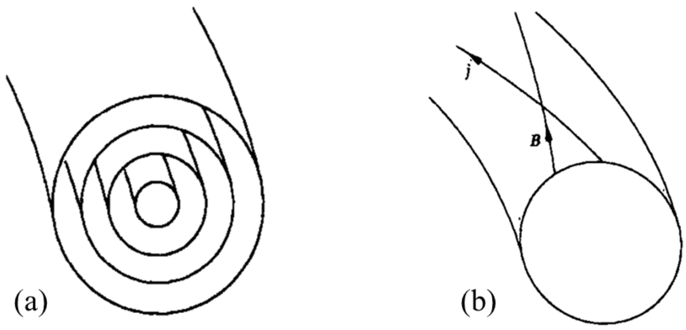

Figure 1.2. (a) Layers of nested magnetic surfaces in tokamak. (b) Magnetic field lines and current lines lie in magnetic surfaces [28].

The basic condition for plasma equilibrium is that the net force at any point in the plasma must be zero, which requires a balance between the magnetic force and the plasma pressure, that is $j \times B = \nabla p$. It is clear from this equation that $B \cdot \nabla p = 0$, which means there is no pressure gradient along the magnetic field lines and the magnetic surfaces are surfaces of constant pressure. From this equation we can also get $j \cdot \nabla p = 0$, which means the current lines lie in the magnetic surfaces [29].

In order to attain thermonuclear conditions within a tokamak, it is necessary to sustain plasma confinement for a significant duration. The global energy confinement time [28] is defined by

$$\tau_E = \frac{\int \frac{3}{2} n(T_i + T_e) d^3x}{P} \tag{1.1}$$

where P is the total input power. In the lack of instabilities, the confinement characteristics of a toroidally symmetric tokamak plasma are primarily governed by the effects of Coulomb collisions, and the resulting particle and energy transport can be accurately calculated. However, the transport observed in tokamak experiments does not match the calculated values, especially in the case of electron energy transport, which exceeds the theoretical predictions by two orders of magnitude. The observed anomalous transport in tokamak plasmas is thought to be caused by plasma instabilities that result in an increased escape rate of particle and energy. This can happen either through perturbations that enable transport across the nested magnetic surface structure or through a breakdown of this structure, which allows particles and energy to move along magnetic field lines that follow random tracks.

For tokamak plasma with auxiliary heating, their transport behavior can generally be described by the scaling law derived from Goldston. This scaling law [28] has been proved to be applicable over a wide range of parameters, and takes the form

$$\tau_E \propto \frac{B_p^2}{nT} l^{1.8} \tag{1.2}$$

where B_p is the poloidal magnetic field and l is the plasma size.

In the NBI heating experiments on ASDEX, it was firstly discovered that under specific conditions, the plasma confinement state would suddenly improve [30]. The confinement time in this higher confinement state was approximately twice as long as that in the previous lower confinement state. This high-confinement plasma state is called the H-mode, and the previous lower level state is known as the L-mode [31]. The confinement improvement is mainly due to the appearance of an edge transport barrier (ETB), a region at the plasma edge with a better confinement state. Other improved confinement modes have also been found during the experiments, especially those plasma operation involving internal transport barrier (ITB) with hollow current profiles.

1.3 Plasma configuration in a tokamak

As mentioned before, in tokamaks the plasma is confined within nested closed magnetic flux surfaces, and these magnetic flux surfaces are determined by the combined magnetic fields generated by external coils and plasma current in the tokamak. There is a special magnetic flux surface known as the LCFS [32], inside which the MFLs lie on the closed magnetic flux surfaces and do not extend to the outside. However, outside the LCFS, the magnetic surfaces are no longer closed, and hence, MFLs on these magnetic surfaces will eventually intersect with the vessel wall. The plasma region outside of the LCFS is commonly referred to as the SOL [33], which exhibits significant differences in properties compared to the plasma within the LCFS.

There are two methods for determining the position of the LCFS during plasma operation: through the limiter and the divertor. In the limiter plasma configuration, the outer magnetic surface may be interrupted by the surface of the limiter, thereby defining the position of the LCFS, as shown in figure 1.3(a). In the divertor plasma configuration, divertor coils can create a null in the poloidal magnetic field near the divertor, thus separating the open and closed magnetic surfaces, as shown in figure 1.3(b).

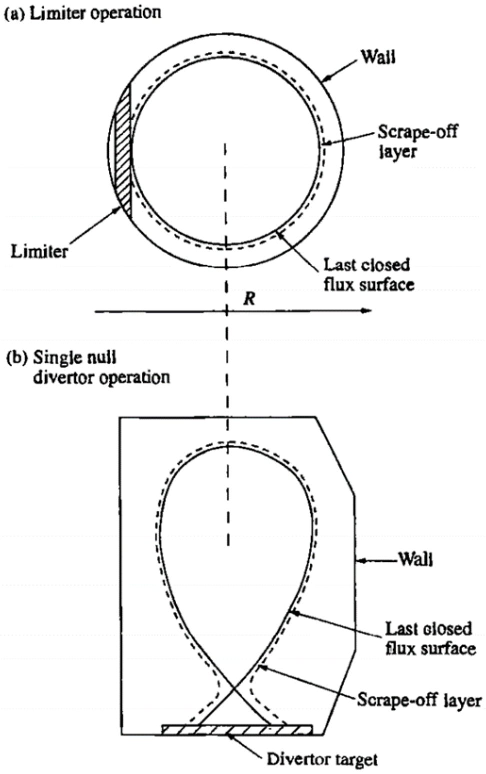

Figure 1.3. Schematic diagram of the scrape-off layer (a) in a limiter configuration and (b) in a poloidal divertor configuration [28].

To better understand the plasma configuration in tokamaks, several fundamental concepts are presented and elucidated as below. Initially, the length $dR_{sep} = R_{sep\,L} - R_{sep\,U}$ [34] is defined, where $R_{sep\,U}$ and $R_{sep\,L}$ represent the upper and lower separatrix radiuses, both can magnetically connected to the middle plane in the low-field side (LFS). In the USN magnetic configuration, the upper X-point denotes the primary X-point, which is the point where the upper separatrix converge. And the primary (secondary) separatrix is the upper (lower) separatrix. Thus, in the USN case the magnitude of dR_{sep} is greater than zero. The primary (secondary) strike point (SP) indicates the point of the primary (secondary) separatrix and the divertor surface converge, respectively. For discharge with USN configuration, two primary strike points located on the outside and inside surfaces of the upper divertor, and two secondary strike points located on the outside and inside surfaces of the lower divertor. The $gapout$ is refers to the length from the first wall to the primary separatrix in the outer middle plane. dR_{mid} is the length from the first wall to the secondary separatrix in the outer middle plane. Figure 1.4 shows a diagram of these definitions. The connection between the dR_{sep}, dR_{mid} and $gapout$ can be mathematically expressed as follows:

$$gapout = \left|dR_{sep}\right| + dR_{mid} \tag{1.3}$$

For the lower single null (LSN) magnetic configuration, the upper (lower) X-point is defined as the secondary (primary) X-point, and the value of dR_{sep} is negative. In the case of a double null (DN) magnetic configuration, the upper and lower separatrices exhibit a high degree of overlap, resulting in dR_{sep} approximately equal to 0. In the EAST tokamak, the secondary X-point is observed within the vacuum vessel, leading to alterations in the magnetic topology in its vicinity.

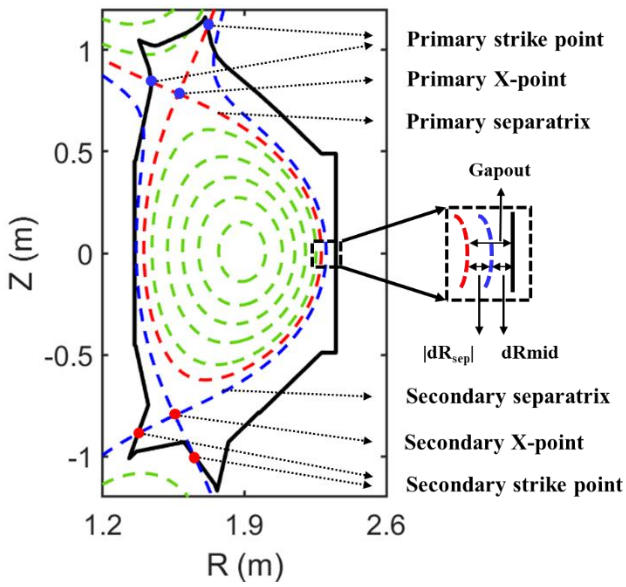

Figure 1.4. The upper single null configuration for EAST discharge #73 993 at 6 s [35].

1.4 Hot spot induced by radio frequency power injection

During plasma operation, excessive local heat loads are sometimes generated on the PFCs. Hot spot, as one of the manifestations of excessive local heat load, is the consequence of interactions between plasma and PFCs, often impeding the sustainment of high-performance plasmas due to undesirable impurity emissions. Furthermore, hot spots can induce the melting of PFCs, leading to severe damage to the machine. Figure 1.5 shows an example of hot spots formation on the PFCs in the EAST 2022 campaign.

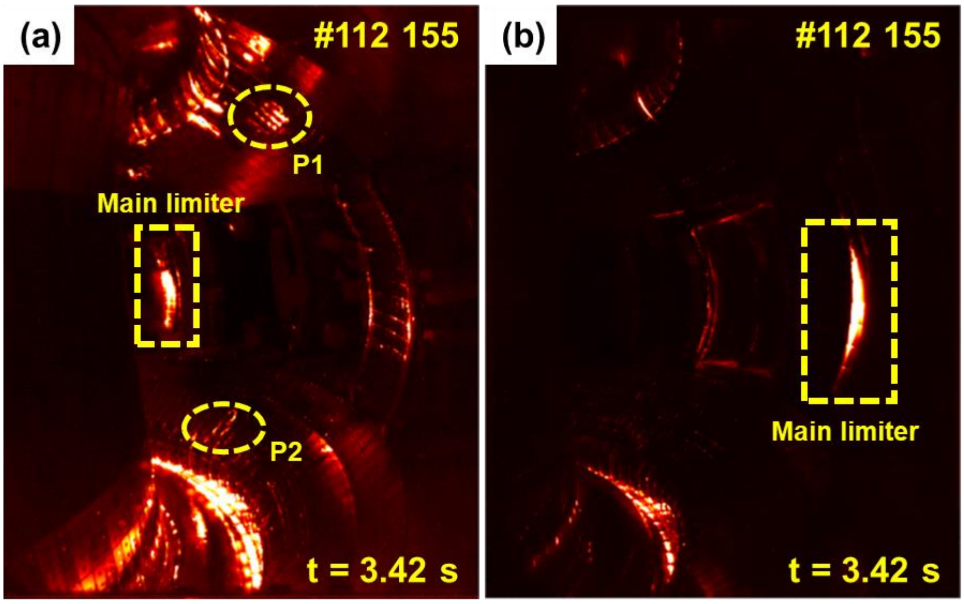

Figure 1.5. Photograph of PFCs for discharge #112 155 at 3.42 s, obtained using an infrared camera. Hot spots on P1, P2 and the main limiter.

The occurrence of hot spots resulting from different RF power injections have been extensively observed in various devices, and subsequent analyses have been performed. In the JET experiment, notable instances of hot spots were noticed both on the ICRF antenna as well as in close proximity to the power antenna on the limiters [36]. These observations were attributed to amplified heat loads arising from the speeding up of ions within the electric field. This electric field is enhanced by the imprecise alignment of the antenna guard elements and the combined magnetic fields [37]. A significant portion of the heat flux deposited on the PFCs in the QUEST tokamak is attributed to the direct loss of energetic electrons, which substantial deviate from the magnetic surface within the ECW heating dominated plasma [38]. In EAST tokamak, the introduction of argon gas puffing during experiment led to a notable reduction in heat flux at the strike point on the lower outer divertor plate, accompanied by a corresponding increase in heat flux at the nearby hot spot region. This observed phenomenon was attributed to the enhanced absorption of LHW in the SOL induced by the argon gas puffing [39]. A comprehensive investigation was conducted on NSTX with high-harmonic fast-wave (HHFW) injection, revealing inspiring insights. The study demonstrated that HHFW power could be coupled to the entire plasma region outside the LCFS, and the MFLs exhibit connectivity between the hot spot and the plasma region outside the LCFS in front of the RF antenna [40]. These studies suggest that hot spots could originate from the transport of electrons follow MFLs in the entire plasma region outside the LCFS, and ultimately impacting the PFCs.

LHW has emerged as a prominent technique for electron heating and plasma current driving, finding widespread utilization in long-pulse operations across various tokamaks [41]. However, the occurrence of hot spots has also become a frequent observation in numerous LHW injection experiments, like in Tore Supra [42], TdeV [43], JET [36, 44], and EAST [39, 45]. Hot spot formation leads to significantly high energy loads on the corresponding plasma facing materials. Regarding the deposition of lower hybrid wave power in the plasma region outside the LCFS, three potential mechanisms have been identified and taken into consideration.

The first mechanism, known as electron Landau damping [46], involves the coupling of large parallel refractive index parts ($N_{\|}$) of the injected lower hybrid wave with the plasma in close proximity to the lower hybrid wave antenna, which results in the heating of electrons. The heated electrons in turn interact with the smaller $N_{\|}$ parts of the injected LHW, leading to further heating. As a result, low-energy electrons in the SOL, typically around 20 eV in energy, can be heated to several keV [47]. The hot spot appearance on the guard limiter of Tore Supra has been attributed to the generation of fast electrons through the parasitic absorption of large $N_{\|}$ lower hybrid wave spectrum

[48]. By employing self-consistent particle-in-cell simulations, it is possible to quantitatively calculate a radial deposition width of several millimeters.

The second mechanism of power deposition associated with LHW is referred to as collision damping [49]. This mechanism primarily occurs in the plasma edge characterized by low electron temperature. Collision damping plays a significant role in wave damping as it hinders a portion or even the majority of LHW power from arriving the plasma region inside the LCFS, where Landau damping is anticipated. To assess the impact of collision absorption on the performance of lower hybrid current drive (LHCD), a combination of experimental data and simulation using a ray-tracing/Fokker–Planck model can be employed. This approach provides an understanding of the LHCD experiments conducted on the FTU tokamak [49].

The third mechanism can be elucidated by the phenomenon known as parametric decay instability (PDI) [50], which induces spectral widening of the wave that was initially launched. This widening leads to a power deposition profile that is more peripheral, via the mechanisms of electron Landau damping and collision damping described above. By incorporating the PDI influence into the ray-tracing/Fokker–Planck model, more precise simulations of the deposition situation of the LHW could be achieved. These delicate simulations provide valuable insights into the sustained long-lasting internal transport barriers observed during lower hybrid current drive experiments conducted on the JET tokamak [51].

The above investigations have made significant contributions to the understanding of RF wave deposition in the plasma region outside the LCFS and the reason of hot spot formation. These findings highlight the importance of two key factors for the hot spot generation during long-pulse plasma operations, namely the physics parameters in the plasma region outside the LCFS and RF energy deposition in this region. The physics parameters in the plasma region outside the LCFS influence the absorption of RF power in this region, which serves as a critical energy source for hot spot generation. While the magnetic topology outside the LCFS is a significant parameter, and its impact on hot spot generation has received only limited attention thus far. Effective prevention of hot spot formation is of paramount importance for achieving longer duration plasma operation. In this thesis, a series of configuration-control experiments were conducted to investigate the influence of SOL magnetic topology on hot spot formation, with magnetic field line tracing outside the LCFS providing intuitive physical images. The results of this research have significantly contributed to the attainment of the longest H-mode discharge in EAST [52].

1.5 Motivation and objective

The pursuit of steady-state operation in magnetic confinement fusion devices represents a fundamental objective within the field of fusion research. Numerous attempts have been made to achieve this goal on various tokamaks, including JET [53], Tore Supra [54], JT-60U [55], TRIAM-1M [56], KSTAR [57], EAST and QUEST [58], yielding highly promising outcomes. QUEST and EAST are among the few tokamaks in the world that can achieve long-pause steady-state operation, to approach the requirements of future fusion reactors. In the future fusion power plant, the plasma is only a heat source in the electricity production process and the generated energy should be completely clarified for the safety of the plant operation, because a little heat load could cause a serious damage to the device. The heat load on the PFCs should be controlled within tolerable limits and excessive local heat load should be avoided. The motivation of this research is to investigate the cause of excessive local heat load on current tokamak, such as EAST and QUEST, in order to accumulate experience for the safe and steady-state operation of current tokamaks and future fusion power plants.

The formation of hot spots is the result of the interaction between the plasma and plasma facing components, significantly impeding the sustenance of high-performance plasmas due to the undesired emission of impurities. Notably, this phenomenon has been observed in one of the longest H-mode experiments achieved on the EAST [59]. Furthermore, the occurrence of hot spots can lead to the meltdown of the plasma facing materials, resulting in severe damage to the fusion device. In EAST, unwanted hot spots sometimes appeared in the lower divertor. This thesis detailed analyzes the mechanism of hot spot generation and the impact of hot spot appearance on the energy load distribution between different plasma facing components.

Carrying substantial amounts of energy, energetic electrons may escape the confinement of the magnetic field and eventually attack the plasma facing components, which might cause damage to the PFCs and threaten the device safety. And a large number of energetic electrons have been found and researched in the QUEST discharge [60, 61]. QUEST is a medium sized spherical tokamak and can perform steady state operations with all-metal temperature-controllable plasma facing walls (PFWs) called the "hot wall" [58]. QUEST possesses improved high-beta stability compared to conventional tokamaks, with major radius $R \sim 0.64$ m and minor radius $a \sim 0.4$ m. The 8.2 and 28 GHz RF sources are utilized to achieve the plasma heating. One of the longest pulse discharges in the world was achieved by QUEST lasting ~6 h, with well-controlled wall temperatures utilizing the hot wall [58, 62] and effective feedback control of the H_α [63, 64]. The schematic view of QUEST is shown in figure 1.6.

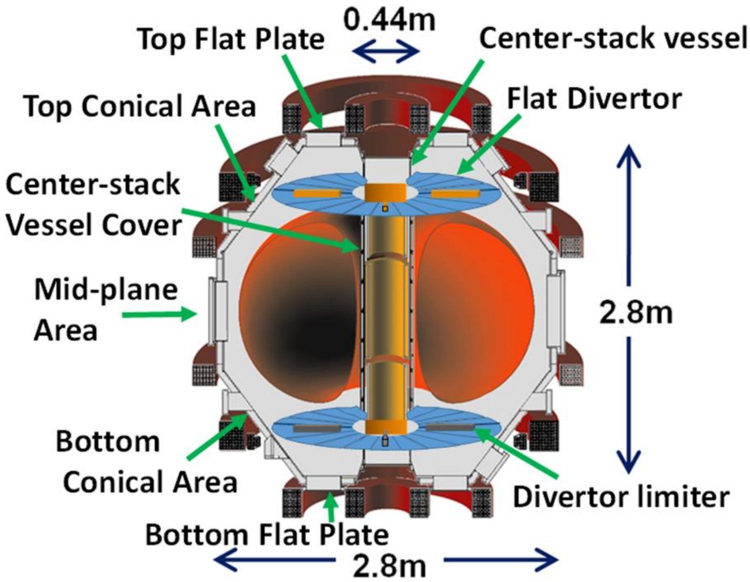

Figure 1.6. Schematic view of QUEST [65].

While the presence of energetic electrons has been observed through many diagnostics systems on QUEST [60, 61], their quantitative characteristics remain difficult to analyze. As one of the effective methods for the above study, particle orbit simulation can provide quantitative features and precise physical images of the particle motion. A series of numerical codes have been developed for the study of particle orbits. However, these codes are primarily used to investigate the confinement and loss of energetic ions, and therefore relativistic effects are not incorporated. But for the research of energetic electrons, relativistic effects is essential and cannot be neglected. Therefore, in this thesis, a novel code called the relativistic guiding center orbit code (RGCO) [66] has been developed and employed to investigate the mechanism of confinement and loss of energetic electrons in the QUEST tokamak. By utilizing the orbit simulation framework in cylindrical coordinates, the code enables particle tracking within the entire vacuum vessel, including the plasma regions both inside and outside the LCFS. Consequently, this approach provides a more realistic assessment of particle confinement and loss compared to previous studies. Simulation results of energetic electron orbits reveals that these electrons can be confined to the main plasma region and the SOL region, within the vacuum vessel of the QUEST tokamak, thereby contributing to non-inductive current driving.

1.6 Thesis organization

The thesis is organized as follows:

In Chapter 1, the operation principle of tokamak and plasma configuration in the tokamak are introduced. With the increasing global demand for energy and the looming energy crisis, the search for sustainable and clean energy sources has become a top priority. Nuclear fusion has the potential to provide nearly unlimited and environmentally friendly energy, so it has gained attention as a promising solution to the energy crisis. Among various fusion confinement methods, tokamak, as a type of magnetic confinement fusion technique, has shown significant prospects for practical applications. As one of the manifestations of excessive local heat load, hot spot formation on PFCs induced by RF heating during plasma operation has been observed on several tokamaks, including EAST and QUEST. Such excessive local heat load poses a significant threat to the safe operation of the device. In order to conduct further research on hot spots observed on EAST and QUEST, a review of this phenomenon is presented.

In Chapter 2, the development and validation of the RGCO code are described. The motion of charged particles in a tokamak can be simplified as a combination of motion along the MFL and Larmor gyration motion perpendicular to the MFL. Full orbit simulation model is based on the real motion of particles in the tokamak, resulting in high accuracy, but it has the drawback of slow tracking speed and high computational resource consumption. On the other hand, guiding center orbit simulation model achieves higher computational speed and good accuracy by simplifying the impact of Larmor gyration motion. The code is based on guiding center orbit tracking formula that incorporates relativistic effects. And the correctness of orbit calculations and relativistic effects in this code were verified through comparison with orbit simulated by other programs. The RGCO code was then used for preliminary studies of energetic electrons in QUEST, and the physical image of energetic electrons being confined in QUEST chamber were demonstrated by the code.

In Chapter 3, an overview of the EAST device is presented. There are five main diagnostics systems for heat load measurement in EAST: calorimetric diagnostics system, infrared (IR) camera, divertor Langmuir probe, thermocouple, and radiation diagnostics system. The calorimetric diagnostics is based on the water-cooling system of PFCs in EAST, and its working principle and data processing methods are described. Furthermore, the water-cooling capacity of the main PFCs in EAST is evaluated using calorimetric measurements.

In Chapter 4, the mechanism of hot spot formation induced by the lower hybrid wave operation in EAST experiments were systematically investigated. It was found that changes of the magnetic configuration in the plasma region outside the LCFS have a significant impact on the hot spot formation, and the formation of hot spots is accompanied by a great variations of energy load distribution among different plasma facing components. These findings also provide an effective solution for mitigating excessive local heat load during LHW injection on EAST.

In Chapter 5, the influence of LHW frequency on the hot spot formation is analyzed. Theoretical calculations reveal that lower frequency of LHW result in more energy deposition on the electrons in the plasma region outside the LCFS due to collision damping. These heated electrons can move along the open MFLs in the plasma region outside the LCFS and eventually impact the PFCs, leading to an increase in heat load on the PFCs. This theoretical analysis is validated through the simulation based on the ray-tracing/Fokker–Planck model.

In Chapter 6, an overall summary and a discussion of the future work are described.

CHAPTER 2. Particle orbit simulation

2.1 Introduction

Energetic particle (EP), generated through auxiliary heating or by the deuterium-tritium reaction, play a significant role in current driving, plasma heating, and momentum injection. Ensuring the effective constraint of energetic particle is crucial for achieving better confinement and safe operation in both current tokamaks and future fusion power plants. The loss of energetic particle can lead to the formation of hot spots and cause severe damage to PFCs. Consequently, a careful investigation of the confinement and loss mechanisms of EP is imperative. During the QUEST discharge, the existence of a considerable population of energetic electrons has also been observed through the Langmuir probe [60] and hard X-ray diagnostics [61], and the research on energetic electrons is ongoing.

Particle orbit simulation serves as an effective complement for the above investigation. Among many optional techniques, the particle-in-cell (PIC) method [67] is employed to track the motion of numerous charged particles within self-consistent electromagnetic fields, making it suitable for addressing plasma instability issues. However, the computational time required by the PIC method becomes unacceptable long when tackling physics issues involving large time ranges, like the deceleration procedure of alpha particles. In such cases, the test particle method emerges as an appealing alternative, which describes the motion of individual particles in an equilibrium electromagnetic field and simulates particle orbit in the same way as the PIC method. Several simulation codes have been developed based on this approach, including NUBEAM [68], ORBIT [69], and ASCOT [70]. These codes were primarily focus on investigating the phase space dynamics of energetic ions, and therefore do not contain relativistic effects. Nonetheless, for such research of energetic electrons, their energy levels are at the same level as those of energetic ions, yet their masses are approximately three orders of magnitude smaller than that of ions, leading to pronounced relativistic effects. Consequently, the development of an orbit simulation code incorporating relativistic effects has become a pressing necessity.

In this context, the development of the RGCO code has been performed. This code conducts orbit simulation of charged particles utilizing cylindrical coordinates, thus enabling a better comprehensive assessment of the confinement and loss of fast electrons inside the whole vacuum vessel. The implementation of the RGCO code represents a significant advancement in the investigation of energetic electron confinement within the QUEST tokamak.

2.2 Single particle orbit motion and full orbit simulation

There are three methods to describe the motion state of plasma. The first method is the single particle orbit description [71, 72], which is also the simplest one, considering only the motion of charged particles in a given electromagnetic field without taking into account the back-reaction of particle motion on the field or the interactions between charged particles. This method provides an intuitive physical picture of the motion of charged particles and serves as a foundation for further research on the complex motion of plasma. The second method is the fluid description [71, 73], where the charged particles in the plasma are treated as an electromagnetic fluid, governed by a self-consistent system of fluid equations and Maxwell's equations. This method can describe the collective interactions and self-consistent fields among charged particles, and it is widely used in plasma physics as many phenomena in plasma can be described using this method. However, the physical quantities in the fluid approach are averaged over fluid elements, thus making it unable to study the velocity distribution of particles within a fluid element. The third method is the kinetic description [72, 74], which considers the velocity distribution function of each species of particles in the plasma.

In the single particle orbit description [71, 72], the motion of a particle with mass m and charge q in a magnetic field B is described by equation 2.1.

$$m\frac{dv}{dt} = qv \times B \tag{2.1}$$

If the magnetic field is uniform and in the z direction, the components of equation 2.1 are

$$\frac{dv_x}{dt} = \omega_c v_y, \qquad \frac{dv_y}{dt} = -\omega_c v_x, \qquad \frac{dv_z}{dt} = 0 \tag{2.2}$$

where $\omega_c = qB/m$ is the cyclotron frequency of the particle. Separation of the variables in equation 2.2 leads to

$$\frac{d^2 v_x}{dt^2} = -\omega_c^2 v_x, \qquad \frac{d^2 v_y}{dt^2} = -\omega_c^2 v_y \tag{2.3}$$

and the solutions of equation 2.3 can be written as

$$v_x = v_\perp \, sin\omega_c t, \qquad v_y = v_\perp \, cos\omega_c t \tag{2.4}$$

Using $v_x = dx/dt$ and $v_y = dy/dt$, equation 2.4 can be integrated to give

$$x = -\rho \, cos\omega_c t, \qquad y = \rho \, sin\omega_c t \tag{2.5}$$

where $\rho = \frac{v_\perp}{\omega_c} = \frac{m v_\perp}{qB}$.

Therefore, in the direction perpendicular to the magnetic field, the particle undergoes circular motion (Larmor gyration motion) with a cyclotron radius ρ (Larmor radius), and moves with a constant velocity in the direction parallel to the magnetic field. And the orbit simulation that includes Larmor gyration motion is referred to as full orbit simulation. In cylindrical coordinate system, the full orbit motion of a particle can be expressed as

$$\begin{gathered} \frac{dR}{dt} = v_R, \qquad \frac{d\phi}{dt} = \frac{v_\phi}{R}, \qquad \frac{dZ}{dt} = v_Z \\ \frac{dv_R}{dt} = \frac{q}{m}\left(v_\phi B_Z - v_Z B_\phi\right) + \frac{v_\phi^2}{R} \\ \frac{dv_\phi}{dt} = \frac{q}{m}\left(v_Z B_R - v_R B_Z\right) - \frac{v_R v_\phi}{R} \\ \frac{dv_Z}{dt} = \frac{q}{m}\left(v_R B_\phi - v_\phi B_R\right) \end{gathered} \tag{2.6}$$

The full orbit model incorporates both Larmor gyration motion and guiding center drift motion, resulting in a more accurate description of particle orbit. However, the calculation of particle full orbit is time consuming.

2.3 Relativistic guiding center orbit code (RGCO)

2.3.1 Equilibrium and perturbation magnetic fields

Due to the absence of a closed magnetic surface in the SOL, particles within this region exhibit a tendency to move along the MFLs and hit the PFCs. This leads to the accumulation of excessive localized heat load, a scenario that future fusion power plants strive to avoid. To facilitate the calculation of particle orbits within the SOL, the code employs cylindrical coordinates as the selected coordinate system.

In order to conduct accurate particle orbit research, both equilibrium and perturbation magnetic fields must be obtained and incorporated into the simulation. The equilibrium magnetic field can be calculated from the poloidal flux Ψ_P and poloidal current function f provided by the Equilibrium Fitting (EFIT) code [75, 76], the Ψ_P is defined in a two-dimensional uniform (R, Z) grid and $f = RB_\phi$ is defined in a one-dimensional uniform Ψ_P grid. The poloidal plot of the Ψ_P in QUEST discharge #35 442 at 2.5 s has been presented in figure 2.1. The radial and vertical components of the poloidal magnetic field can be determined using the following equations [77].

$$B_R(R,Z) = -\frac{1}{2\pi R}\frac{\partial \Psi_P(R,Z)}{\partial Z} \tag{2.7}$$

$$B_Z(R,Z) = \frac{1}{2\pi R}\frac{\partial \Psi_P(R,Z)}{\partial R} \tag{2.8}$$

By employing this approach, the equilibrium magnetic field satisfying the divergence-free condition is acquired, serving as the fundamental requirement for precise orbit calculations.

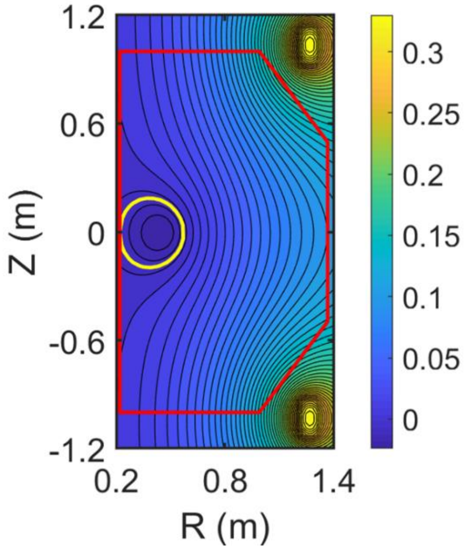

Figure 2.1. The poloidal plot of the Ψ_P in QUEST discharge #35 442 at 2.5 s. The red line corresponds to the boundary of the first wall within the QUEST device, while the yellow circle indicates the location of the LCFS [66].

The ripple magnetic field, arising from discrete toroidal field coils, is recognized as a significant perturbation magnetic field. It poses a risk of inducing classical particle loss through the diffusion of banana orbits, wherein the turning points of these orbits are situated within a specific zone in close proximity to the top and bottom regions. Consequently, when designing a new tokamak, the ripple magnetic field emerges as a crucial engineering parameter that necessitates careful consideration. Incorporating the ripple magnetic field into the simulation, the toroidal magnetic field can be computed using the following equation [78].

$$B_\phi(R,Z) = B_{\phi 0}(R,Z) + B_{\phi 0}(R,Z) * \delta(R,Z) * \cos(\phi) \tag{2.9}$$

where

$$\delta(R,Z) = (B_{max} - B_{min})/(B_{max} + B_{min}) \tag{2.10}$$

The first term on the right-hand side of equation 2.9 represents the equilibrium magnetic field, while the second term corresponds to the ripple magnetic field. Here, δ denotes the ripple magnitude at a specific location within the tokamak. To determine δ, the maximum value of $B_\phi(R,\phi,Z)$ is obtained on the $R-Z$ plane coinciding with the location of the toroidal field (TF) coil ($\phi = 0$). Similarly, B_{min} is acquired on the plane situated in the middle of two $R - Z$ planes where the two TF coils are positioned ($\phi = \pi/N_{coil}$). The value of the magnetic field at any given location within the tokamak can be estimated using the Biot-Savart Law. By combining equation 2.10, the ripple present in the tokamak can be evaluated. Figure 2.2 illustrates the ripple of the QUEST tokamak, revealing a negligible ripple magnitude within the vacuum vessel of the QUEST device.

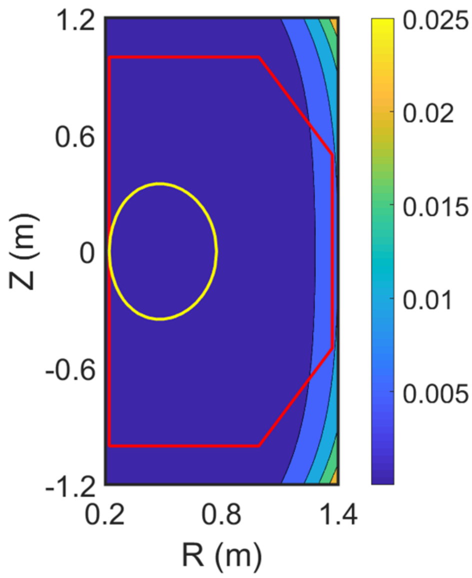

Figure 2.2. The value of ripple exhibited in the QUEST tokamak. The red line corresponds to the boundary of the first wall, while the yellow circle indicates the position of the LCFS [66].

2.3.2 Motion equation and solution algorithm

The equation for guiding center orbit motion is more complex compared to the full orbit motion equation, but the computational efficiency is greatly improved by reasonably averaging the effect of the Larmor gyration motion. The equations of guiding center orbit motion without relativistic effects [79] are expressed as

$$\frac{d\vec{X}}{dt} = \frac{\vec{B}^*}{B_\parallel^*} v_\parallel + \frac{\mu}{m\Omega B_\parallel^*} \vec{B} \times \nabla B + \frac{1}{BB_\parallel^*} \vec{E} \times \vec{B} \tag{2.11}$$

$$\frac{dv_\parallel}{dt} = -\frac{\mu}{m} \frac{\vec{B}^*}{B_\parallel^*} \cdot \nabla B + \frac{Ze}{m} \frac{\vec{B}^*}{B_\parallel^*} \cdot \vec{E} \tag{2.12}$$

In the above equations, the guiding center position of particle motion, denoted as X, can be decomposed into three components within the cylindrical coordinate system: R, ϕ, Z. The parallel velocity of the particle with respect to the magnetic field is represented as $v_\parallel$, while m and Ze correspond to the mass and charge of the particle, respectively. The magnetic moment is defined as $\mu = mv_\perp^2/2B$, where $v_\perp$ denotes the perpendicular velocity of the particle relative to the magnetic field. Additionally, $\Omega = BZe/m$ signifies the cyclotron angular frequency. Equation 2.11 contains the curvature drift, ∇B drift, and $E \times B$ drift of the charged particle motion. The quantities $\vec{B}^*$ and $B_\parallel^*$ are introduced and defined as follows, where $\vec{b} = \vec{B}/B$.

$$\vec{B}^* = \vec{B} + B\frac{v_\parallel}{\Omega}\nabla \times \vec{b} \tag{2.13}$$

$$B_\parallel^* = \vec{b} \cdot \vec{B}^* = B(1 + \frac{v_\parallel}{\Omega}\vec{b} \cdot \nabla \times \vec{b}) \tag{2.14}$$

In the case of energetic particles, particularly fast electrons, which can attain velocities close to the speed of light due to the auxiliary heating systems employed in tokamaks, such as LHW and ECRH. The confinement of fast electrons becomes a critical concern. At such elevated energy levels, these electrons may experience confinement loss, leading to interactions with the PFCs and resulting in excessive localized heat deposition on the PFCs. This poses a significant challenge to achieving steady-state operation in future fusion power plants. Consequently, investigating the confinement mechanisms of energetic particles becomes imperative. The motion of guiding center orbits for particles subjected to relativistic effects [66, 80] can be described as follows (assuming the absence of electric field)

$$\frac{d\vec{X}}{dt} = \frac{\vec{B}^*}{B_\parallel^*}\frac{p_\parallel}{m\gamma} + \frac{\mu}{m\Omega B_\parallel^*}\vec{B} \times \nabla B \tag{2.15}$$

$$\frac{dp_\parallel}{dt} = -\mu\frac{\vec{B}^*}{B_\parallel^*} \cdot \nabla B \tag{2.16}$$

where $p_\parallel = \gamma m v_\parallel$ represents the relativistic parallel momentum, while $\vec{B}^*$, $B_\parallel^*$ and the relativistic factor γ are defined as follow

$$\vec{B}^* = \vec{B} + B\frac{p_\parallel}{\mathrm{m}\Omega}\nabla \times \vec{b} \tag{2.17}$$

$$B_\parallel^* = \vec{b} \cdot \vec{B}^* = B(1 + \frac{p_\parallel}{\mathrm{m}\Omega}\vec{b} \cdot \nabla \times \vec{b}) \tag{2.18}$$

$$\gamma = \sqrt{1 + \frac{2\mu B}{mc^2} + \frac{p_\parallel^2}{m^2c^2}} \tag{2.19}$$

The aforementioned equations are employed in the code to trace the orbits of charged particles. Equations 2.15 and 2.16 represent typical ordinary differential equations (ODEs), and to ensure a minimal numerical error at each time step, the fourth-order Runge-Kutta method (RK4) [81, 82] is utilized to numerically solve these ODEs. The fundamental equations for RK4 are presented as follows

$$\begin{gathered}
k_1 = hf(x_n, y_n) \\
k_2 = hf(x_n + \frac{h}{2}, y_n + \frac{k_1}{2}) \\
k_3 = hf(x_n + \frac{h}{2}, y_n + \frac{k_2}{2}) \\
k_4 = hf(x_n + h, y_n + k_3) \\
y_{n+1} = y_n + \frac{k_1}{6} + \frac{k_2}{3} + \frac{k_3}{3} + \frac{k_4}{6} + O(h^5)
\end{gathered} \tag{2.20}$$

where h represents the step length employed in the calculation. To guarantee the accuracy of the orbit calculation, a rectangular mesh grid of 200×200 is generated in the $R - Z$ plane. The magnitude of magnetic field at the particle location is acquired using the cubic spline interpolation method. With these preparations in place, the particle orbit can be computed iteratively.

2.3.3 Benchmark of the code

The first step involves utilizing a previously published guiding center orbit simulation code (without considering relativistic effects) [83] to validate the accuracy of the newly developed RGCO. In this validation process, an electron with 100 eV is selected as the test particle, with relativistic effects being negligible. The motion trajectory of the test particle within the EAST equilibrium is calculated using both the RGCO and the test code. Subsequently, the obtained orbits are decomposed into three orthogonal components within the cylindrical coordinate system: $R-t, \phi-t, Z-t$. Figure 2.3 presents these orbits. The remarkable sameness of the trajectories computed by the RGCO and the test code in all three directions strongly suggests the capability of the RGCO in accurately calculating particle orbits.

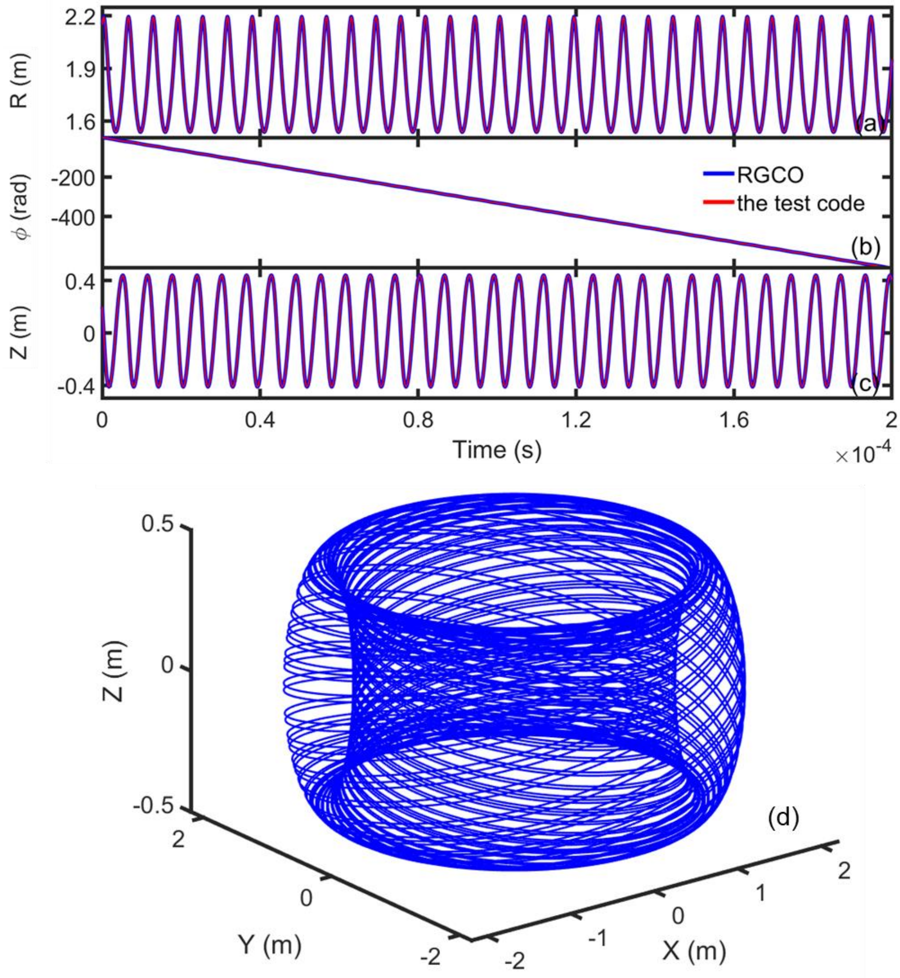

Figure 2.3. The motion trajectory of electron within the EAST tokamak is computed using both the RGCO (depicted in blue) and the test code (depicted in red). The initial conditions of the test particle are set as follows: position $(R, \phi, Z) = (2.15\ \mathrm{m}, 0, 0.2\ \mathrm{m})$, pitch angle of 0°, and particle energy of 100 eV. The resulting orbits are decomposed into three distinct components (a): $R-t$, (b): $\phi-t$, and (c): $Z-t$. (d): A three-dimensional view of the orbit computed by the RGCO.

The next step involves assessing the accuracy of relativistic effects within the RGCO. To perform this evaluation, fast electron is chosen as the test particle with initial pitch angles of 0° and 30°, possessing high energy of 1 MeV, considering the non-negligible influence of relativistic effects on such particle. Both codes are employed to calculate the motion trajectory of the test particle. The outcomes are illustrated in figure 2.4. It is evident that neglecting the relativistic effects leads to an increase in electron velocity, resulting in accumulated errors over the simulation time steps. Furthermore, the pitch angle significantly impacts the trajectory of the particles. Through the two-step validation, it is confirmed that the RGCO is suitable for particle orbit simulations, including energetic particles.

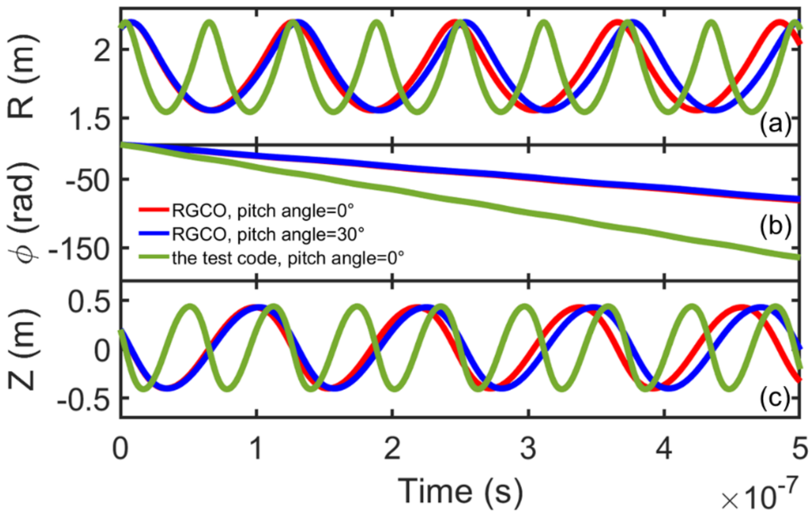

Figure 2.4. The trajectory of energetic electrons in EAST equilibrium is calculated. The initial conditions of the test particle include its position at $(R, \phi, Z) = (2.15\ \mathrm{m}, 0, 0.2\ \mathrm{m})$ and its energy of 1 MeV. The orbit calculation by RGCO with initial pitch angle 0° (represented by the red curve), with initial pitch angle 30° (represented by the blue curve), calculated by the test code with initial pitch angle 0° (represented by the green curve). The decomposition of the orbits into three different components is presented in: (a) $R - t$, (b) $\phi - t$, and (c) $Z - t$.

2.3.4 Energetic electron orbit simulation in QUEST

Despite the toroidal symmetry of the EFIT equilibrium in a tokamak, the motion of electrons within the plasma is inherently three-dimensional. Various auxiliary systems employed for plasma operation, such as auxiliary heating systems and RMP coils, are positioned at different toroidal locations within the tokamak. Consequently, the local electron motion can be influenced by these systems. To account for this, a three-dimensional flexible geometric model is implemented in the code. For instance, the model can incorporate features like the LHW guard limiter in EAST and the movable limiter in QUEST. When a particle reaches these kinds of boundaries, the orbit tracking is automatically terminated and the termination position is recorded. By assigning different boundary conditions in distinct simulation cases, various physics phenomena can be explored, including the formation of hot spots and the confinement of energetic particles.

Experimental evidence has demonstrated the excitation and maintenance of energetic electrons in QUEST plasma through the utilization of 2nd harmonic ECRH [61]. In order to investigate the confinement characteristics of these energetic electrons during such experiments, an energetic electron orbit simulation employing the RGCO code is conducted. The required plasma equilibrium for the RGCO code is provided by the EFIT code. Using the magnetic reconstruction data from discharge #35 442 at 2.5 s, the forward-tracking of electron orbits is carried out both inside and outside the LCFS. A pitch angle scan is performed, ranging from 0° to 180° at 10° intervals. The initial energy of the electrons is set to 20 keV, representing the average energy of the tail electrons observed in this discharge [61].

The initial location of the test particle within the LCFS is defined in cylindrical coordinates as $(R, \phi, Z) = (0.55\ \mathrm{m}, 0, 0\ \mathrm{m})$. Figure 2.5 illustrates the electron orbit simulations for various pitch angles, utilizing the RGCO code. Notably, the observations reveal distinct behaviors: when the pitch angle ranges between 0° and 40° or between 140° and 180°, the electron follows a passing orbit, whereas a banana orbit is followed when the pitch angle ranges from 50° to 130°. The shape of the banana orbit demonstrates systematic changes with alterations in the pitch angle. As the pitch angle increases from 50° to 90°, the width of the banana orbit gradually diminishes from approximately 1 cm to about 0.02 cm. Simultaneously, the poloidal extent occupied by the banana orbit gradually contracts, and all orbits exhibit an inward shift. Conversely, as the pitch angle increases from 90° to 130°, the width of the banana orbit progressively expands from around 0.02 cm to approximately 1 cm. Additionally, the poloidal range encompassed by the banana orbit gradually increases, resulting in outwardly shifting orbits. Notably, all electrons with varying pitch angles can be confined within the LCFS.

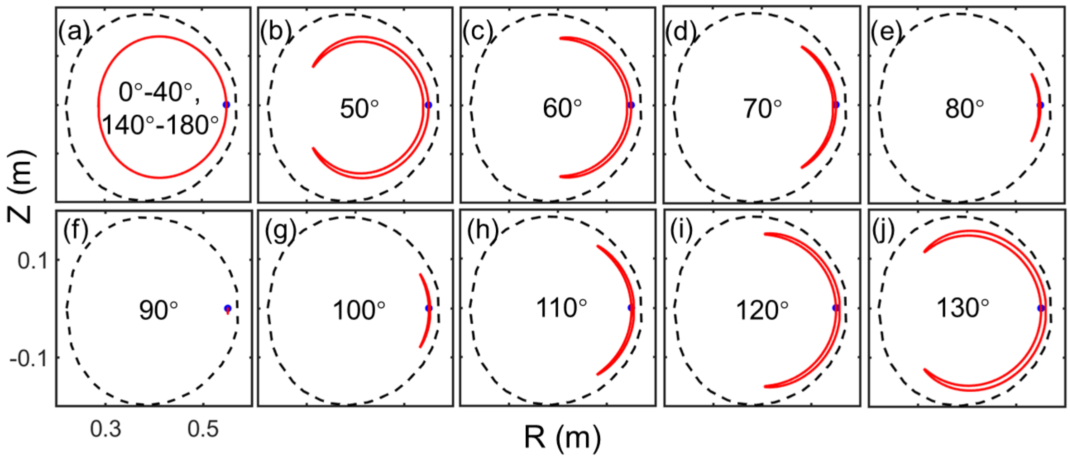

Figure 2.5. The motion of energetic electrons within the LCFS exhibits different orbit patterns. In each subplot, the red curve represents the electron orbit characterized by a specific pitch angle, while the black dotted curve represents the LCFS boundary. Additionally, the blue dot corresponds to the initial starting point of the orbit [66].

After the orbit analysis within the LCFS, electron orbit simulations are conducted outside the LCFS as well. The initial location of the test particle is specified as $(R, \phi, Z) = (0.8 \text{ m}, 0, 0 \text{ m})$. Figure 2.6 portrays the simulations of electron orbits for different pitch angles, implemented using the RGCO code. Notably, distinct behaviors are observed depending on the difference in pitch angle. For pitch angles ranging between 0° and 50°, electrons exhibit an upward trajectory that ultimately leads to hitting the PFCs. This phenomenon has the potential to induce a heat load on the upper divertor. Conversely, when the pitch angle falls within the range of 130° to 180°, electrons move in a downward direction and ultimately hit the lower divertor, which may result in heat load on the lower divertor. Within the pitch angle range of 60° to 120°, electrons follow a banana orbit, thereby remaining confined by the magnetic field.

Similar to the banana orbit observed within the LCFS, the shape of the banana orbit outside the LCFS exhibits analogous patterns when the pitch angle undergoes variation.

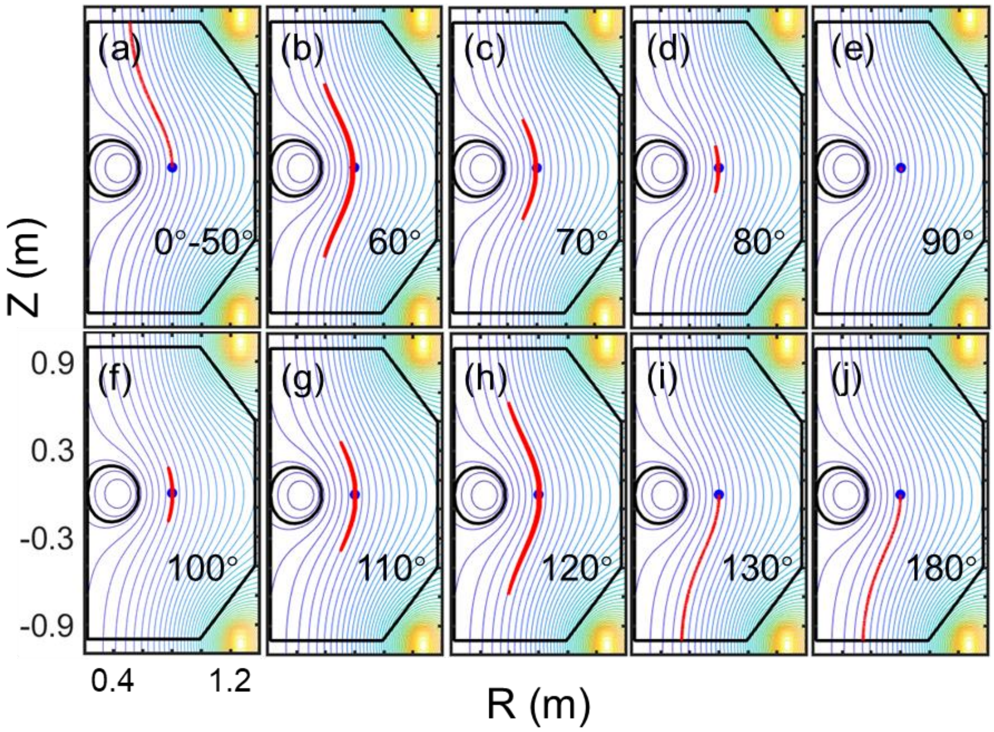

Figure 2.6. The motion of energetic electrons outside the LCFS exhibits different orbit patterns. In each subplot, the red curve represents the electron orbit associated with a specific pitch angle. The LCFS is depicted as a black circle, while the blue dot signifies the initial starting point of the orbit [66].

The obtained simulation results provide confirmation that energetic electrons can be confined within the plasma, thereby contributing to the non-inductive current driving of the QUEST discharge. However, this discharge was performed in 2017 QUEST campaign, the water-cooling data for the PFCs were not preserved, and moreover, this discharge lasted only a few seconds. Therefore, it was hard to conduct the study of heat load distribution and hot spot formation in this discharge. But as a powerful tool to research particle motion, RGCO has been developed. The next step is to study the topics related to energetic electrons in QUEST, such as the confinement of energetic electrons and the hot spot formation caused by the energetic electrons, through the combination of experiment data and RGCO code simulation.

2.4 Conclusion

EP physics constitutes a vital area of study in magnetic confinement fusion research. In order to gain a deeper understanding of the confinement and loss mechanisms governing energetic electrons in spherical tokamaks, a novel numerical code called RGCO has been developed. This code incorporates relativistic effects and operates on the basis of the test particle method. It enables the orbit simulation within a cylindrical coordinate system, taking into account the realistic tokamak geometry, including the first wall as a tracking boundary, as well as the three-dimensional magnetic field encompassing the ripple magnetic field. The presented simulation results obtained using the RGCO code provide evidence for the confinement of energetic electrons within the tokamak magnetic configuration. This confinement is observed both inside and outside the LCFS, and it is influenced by the pitch angle.

Alpha particles, with an energy of 3.5 MeV, hold significant importance as a prominent product in D-T nuclear fusion reactions. Their role is crucial in achieving self-sustained burning within future fusion power plants. Consequently, the investigation of the confinement and loss mechanisms governing alpha particles represents a fundamental aspect of research in this field. And the research on energetic electron in QUEST, through the combination of physics experiment and RGCO code simulation, will serve as the foundation for the related study of alpha particle.

CHAPTER 3. Experimental apparatus and diagnostic techniques

3.1 EAST tokamak

EAST, a medium-sized superconducting tokamak, adopts magnetic configurations similar to ITER, featuring a major radius (R) of 1.85 m, a minor radius (a) of 0.45 m, a plasma current (I_P) of 1 MA, and a toroidal field (B_T) of 3.5 T [84, 85]. EAST employs actively water-cooled metallic PFCs, following the design principles applied in ITER [86-88] and CFETR [89-91]. Figure 3.1 provides a comprehensive view of the EAST facility, with the main chamber predominantly coated by molybdenum, the upper divertor clad in mono-block tungsten of ITER-grade quality, and the lower divertor clad in graphite, as illustrated in figure 3.2. In early 2021, EAST successfully developed and installed a new lower tungsten divertor, replacing the previous graphite divertor. This upgrade significantly enhanced the power handling capability of the divertor from less than $2\ \mathrm{MW/m^2}$ to approximately $10\ \mathrm{MW/m^2}$ [92]. Consequently, EAST has achieved the utilization of all-metallic PFCs, as demonstrated in figure 3.3.

The principal objective of the EAST tokamak is to attain the stable, long-duration, and high-confinement H-mode plasmas, employing configurations and operation schemes akin to that of ITER. EAST achieved a high-temperature long-pulse plasma operation with an electron temperature exceeded 4.5 keV and a duration of 102 s in 2016 [93], a 101.2 s long-duration H-mode plasma operation in 2017 [59, 94, 95], a 1056 s improved confinement plasma operation with Super I-mode in 2021 [96], and a 403 s long-pulse high-confinement H-mode plasma operation in 2023.

EAST possesses a total of sixteen equatorial ports, labeled as ports A to P in the toroidal orientation, as depicted in figure 3.4. Among these ports, ports N and E are equipped with two distinct sets of LHW systems, LHW 1 and LHW 2, operating at frequencies of 2.45 GHz and 4.6 GHz, as illustrated in figure 3.4.

Figure 3.1. The full view of EAST.

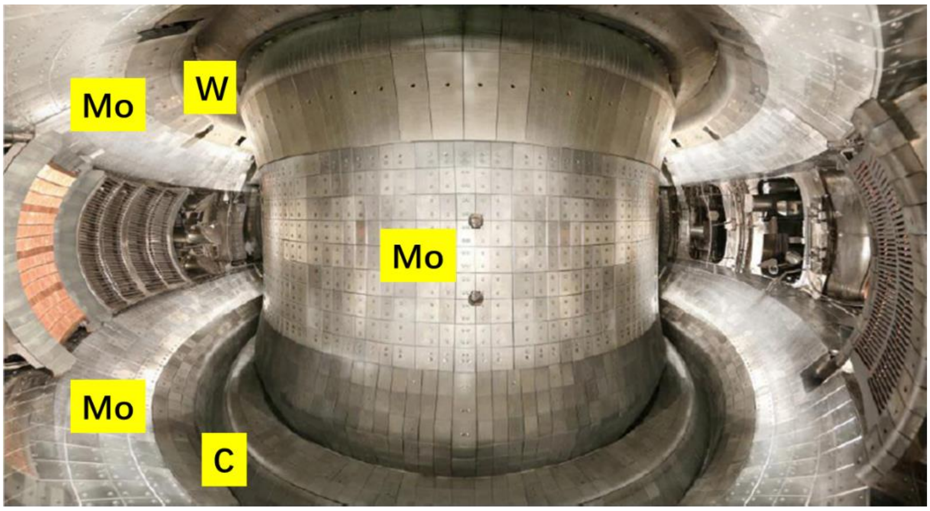

Figure 3.2. Materials of EAST's plasma facing components with graphite lower divertor.

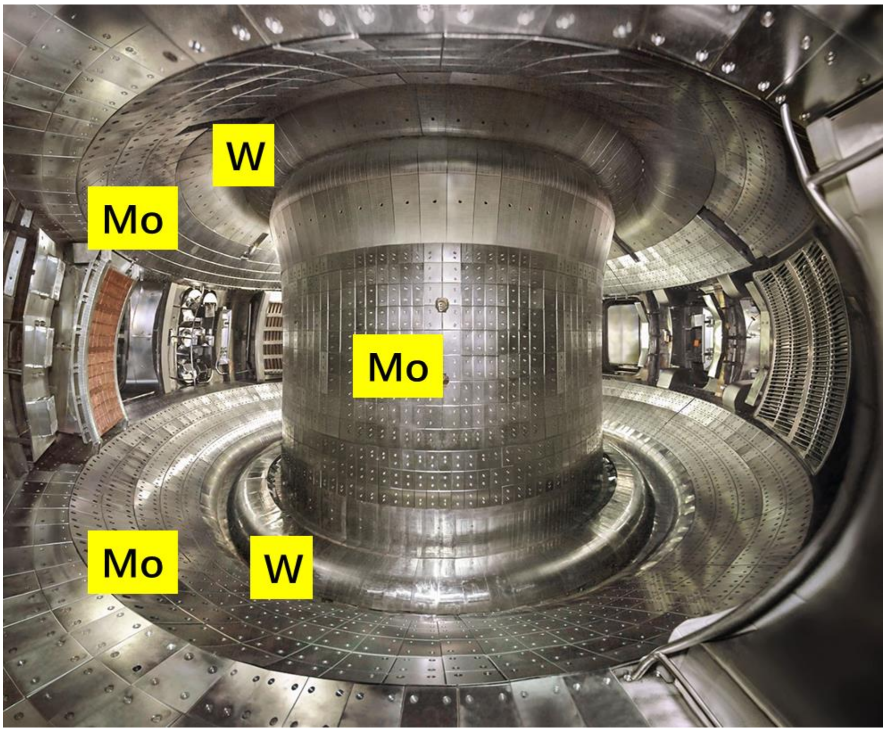

Figure 3.3. Materials of EAST's plasma facing components with tungsten lower divertor.

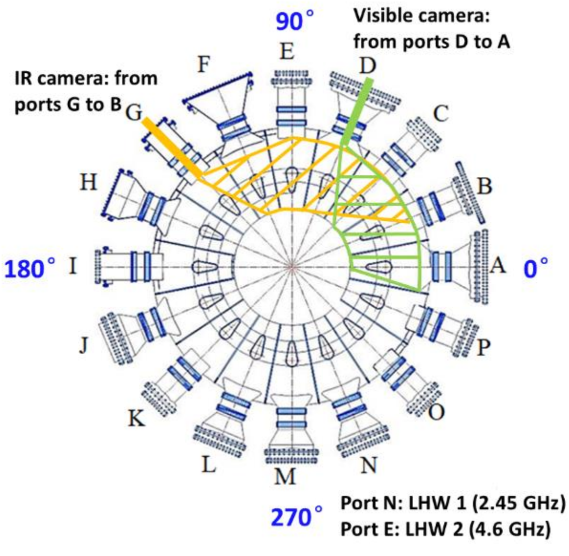

Figure 3.4. The top view of the toroidal arrangement of EAST and the location of the two LHW launchers are depicted. The orange lines represent the field of view (FoV) of the infrared (IR) camera, while the green lines represent the FoV of the visible-light camera [35].

EAST is equipped with a combined power capacity of approximately 32 MW for plasma heating and current driving purposes. This power allocation includes NBI power, contributing around 8 MW, and RF power, accounting for approximately 24 MW. The RF power distribution comprises three components:

(a) LHW, delivering approximately 10 MW in power, with a division of approximately 4 MW at 2.45 GHz and approximately 6 MW at 4.6 GHz.

(b) ECRH, providing around 2 MW of power at the frequency of 140 GHz.

(c) ICRF, supplying approximately 12 MW of power within the frequency range of 27 to 80 MHz.

EAST has the capability to effectively achieve a significant energy injection in steady-state thousand-second operation [96]. This achievement aligns with the objectives of steady-state and long-duration discharge in future fusion devices, such as ITER.

In accordance with the advancements in system upgrades and physics research, a three-phase plan has been developed for EAST [85]. Phase I-a has been successfully achieved after the completion of the systems upgrade.

A. Phase I

a) Achieving 100 s plasma operation under full metal wall, $T_{e0} > 8.5$ keV.

b) Achieving H-mode plasma operation with an energy injection of 1.0 GJ sustained for over 400 seconds, $H_{98y2} > 1.0$.

c) Achieving plasma operation with a total integrated heating power of 10 MW, under full metal wall.

B. Phase II

a) Achieving reactor-oriented operation for a duration exceeding 20 times the current diffusion timescale, typically ranges from 10 to 20 s. In which, q_{95}~6.5, $n_e/n_G = 0.5 - 0.85$, v^*~$0.02 - 0.05$, and T_e/T_i~2.0.

b) Demonstrating a divertor configuration plasma operation with capable of handling heat exhaust at a level of $10\ \mathrm{MW/m^2}$, sustained for a duration of 100 s.

c) Achieving plasma operation of the ITER-baseline-like scenario, with $q_{95}\sim3.0-6.0$, $\beta_N\sim2.0-3.0$, and $H_{98}\sim1.5-2.0$.

C. Phase III

a) Achieving 1000 s timescale plasma operation with high T_e, $T_{e0}>8.5$ keV.

b) Extension of the reactor-oriented operation to 400 s timescale.

3.2 Heat load measurement of plasma facing components (PFCs) in EAST

3.2.1 Introduction

Heat load deposition on the first wall due to the interaction between plasma and PFCs. Excessive local heat load can cause damage to the PFCs, significantly affecting their lifespan and posing a threat to device safety. Excessive local heat load can also cause melting of the first wall material, leading to impurity sputtering. Currently, many fusion experiment devices use tungsten as the plasma-facing material for the first wall due to its favorable properties. However, sputtering of tungsten from the first wall can increase the tungsten content in the main plasma, resulting in increased radiation and decreased plasma performance, or even cooling and disruption of the plasma. Moreover, the sputtered impurity ions can transport parallel to the magnetic field lines, leading to substantial ion bombardment on the first wall. As the retention of fusion fuel particles in the PFCs is related to the temperature of the PFCs, excessive energy load on the first wall can also enhance the recirculation of fuel particles, severely impacting the confinement property of the plasma. Therefore, real-time monitoring of the first wall heat load and timely mitigation of excessive local heat load are crucial for the safe operation of plasma devices.

Currently, EAST possess five diagnostics systems related to heat load measurement, including calorimetric diagnostics [59, 97, 98], infrared camera [99, 100], divertor Langmuir probe [101, 102], thermocouple, and radiation diagnostics [103, 104].

Calorimetric diagnostics system provides accurate measurement of the total heat load on the component during discharges through the measurement of cooling water for the component. However, due to limitations in measurement principles, the time and spatial resolutions of this system are not very high. Cross-validation of energy load measurement between calorimetric diagnostics and IR camera has been completed, achieving excellent results [59].

Infrared camera has advantages such as non-contact measurement, wide temperature measurement range, and fast temperature measurement response. However, its measurement is influenced by factors such as impurity deposition layers, emissivity of materials, viewing angle, background environmental temperature, and transmittance of the optical system.

Divertor Langmuir probe has a simple structure and convenient data processing, and can measure many parameters such as heat flux, electron temperature, and electron density. However, it is susceptible to factors such as magnetic fields, electron velocity distribution, RF fields, and secondary electron emission, and can only measure the heat flux generated by localized electrons and ions.

Thermocouple diagnostics system has a simple structure and easy to use, and has been installed on the first wall. But it is susceptible to factors such as magnetic field interference and poor contact, and requires the use of inverse algorithms [105] to convert the temperature of the measurement point to the heat flux on the component surface [106].

Radiation diagnostics system on EAST consist of the absolute extreme ultraviolet photodiodes diagnostic (AXUV) [103] and the metal foil resistive bolometer system [104], which can measure the radiation power of the entire plasma region, but the energy load deposited on the plasma facing components includes energy loss channels other than radiation.

3.2.2 Infrared camera

The temperature and heat flux are two important heat load parameters for the PFCs during plasma operation, particularly for the divertor target plates. Many nuclear fusion devices, such as EAST [99, 100], HL-2A [107], DIII-D [108], JET [109], JT-60U [110], KSTAR [111], ASDEX-U [112], Alcator C-Mod [113], Tore Supra [114] and NSTX [115, 116], are equipped with infrared cameras for thermal radiation measurement. Thermal radiation is one of the most common forms of electromagnetic radiation in nature, emitted by all objects with a temperature above absolute zero degree in a wide range of wavelengths in all directions. The amount of radiation energy emitted from the surface of an object at a given wavelength depends on the material, surface condition, and surface temperature of the object. Therefore, even at the same surface temperature, different objects may emit different amounts of radiation.

Infrared camera utilizes the detection of thermal radiation emitted by objects to measure their temperatures, based on the theory of blackbody radiation [117]. A blackbody is an idealized object that has the highest radiation power density at a particular temperature and wavelength, while the radiation from real objects is less than that of a blackbody. The Planck's blackbody radiation law is given by:

$$M_b(\lambda,T)=\frac{2\pi hc^2}{\lambda^5}\frac{1}{e^{hc/kT\lambda}-1} \tag{3.1}$$

where h is the Planck constant, c is the speed of light, λ is the wavelength, T is the absolute temperature of the blackbody, and k is the Boltzmann constant. $M_b(\lambda,T)$ is the monochromatic radiance, which represents the radiation emitted per unit time, per unit surface area, per unit wavelength interval, into the entire hemisphere of space around the blackbody, and its unit is $\mathrm{W/m^3}$. Equation 3.1 indicates that an object at a specific temperature T will emit electromagnetic waves of different wavelengths, and a specific wavelength λ corresponds to a specific value of monochromatic radiance. The blackbody radiation power can be obtained by integrating over wavelength in equation 3.1.

$$M_b(T)=\sigma T^4 \tag{3.2}$$

This is known as the Stefan-Boltzmann law, where $\sigma = 5.670 \times 10^{-8}\ \mathrm{W \cdot m^{-2} \cdot K^{-4}}$ represents the Stefan-Boltzmann constant. However, real objects are not perfect blackbodies and their radiation capacity are less than that of a blackbody. Therefore, the emissivity ε of the object is introduced to modify equation 3.2.

$$M_b(T) = \varepsilon \sigma T^4 \tag{3.3}$$

The field of view (FoV) of the IR camera in EAST is depicted in figure 3.4. In the divertor region, the spatial resolution achieved was approximately 4 mm in cases with a large FoV. The frame rate in the full-frame mode was 115 Hz; however, by reducing the FoV, it was possible to increase the frame rate to several kHz.

Although infrared camera is widely used for temperature measurement in the fusion devices due to its high temporal and spatial resolution, there are several factors that can affect the accuracy of temperature measurements, as listed below.

(1) Impact of emissivity:

Emissivity represents the rate of the radiation energy launched from the surface of an object to that of a blackbody at a given temperature. However, the emissivity of a specific material is influenced by surface roughness, surface temperature, and the specific wavelength. In EAST experiment, the heat load from the plasma is mainly deposited on the target plate of the tungsten divertor, but the emissivity of tungsten is relatively low, making it susceptible to the influence of infrared radiation from the background environment.

(2) Impact of background environment temperature:

During temperature measurement of a target object, the radiation energy from surrounding high-temperature objects can be reflected by the target object and detected by the infrared camera, introducing measurement errors. When the emissivity of the target object is low and the reflectivity is high, the measurement error will be larger.

(3) Impact of viewing angle:

The emissivity of the target object is not uniform within different solid angles in space.

Therefore, it is more reasonable to research the surface temperature and energy flux on plasma facing components through the combination of different heat load diagnostics systems.

3.3 Calorimetric diagnostics system

3.3.1 Measurement principle

The EAST possesses a pressurized water system to eliminate the energy load on the PFCs during the plasma operation, which consists of five water-cooling modules. In early 2021, with the upgrade of the lower divertor, the water-cooling systems underwent upgrades as well, as shown in figure 3.5.

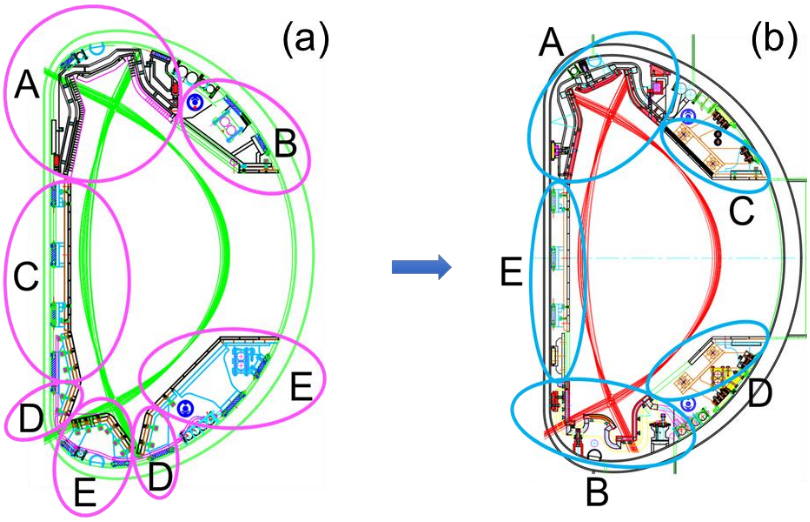

Figure 3.5. The schematic layout of the water-cooling modules in EAST, both before (a) and after (b) the upgrade of lower divertor, is presented in the poloidal cross-section. In the pre-upgrade arrangement (a): module A is responsible for cooling the upper divertor, module B is responsible for cooling the upper passive plate and the upper low-field side PFCs, module C is responsible for cooling the high-field side PFCs, module D is responsible for cooling the lower divertor with inside and outside target plates, and module E is responsible for cooling the lower divertor with the dome part, and part of the first wall on the low-field side. In the post-upgrade arrangement (b): module A is responsible for cooling the upper divertor, module B is responsible for cooling the lower divertor, module C is responsible for cooling the upper part of the first wall on

the low-field side, module D is responsible for cooling the lower part of the first wall on the low-field side, and module E is responsible for cooling the part of the first wall on the high-field side.

The data of the calorimetric diagnostics system are obtained from the temperature sensors and flow meters installed in the water-cooling system of EAST. During discharge, the energy load on the plasma facing components is transferred to the cooling water of the water-cooling system, resulting in an increase in water temperature. The energy load carried away by the cooling water is equal to the energy load on the plasma facing components, and can be calculated as

$$E = CG\rho \int_{t_0}^{t_0+\Delta t} [\, T_{outlet}(t) - T_{inlet}(t) \,]\, dt \tag{3.4}$$

where E is the energy load taken away by the cooling water, C, G and ρ are the specific heat capacity, volume flow rate and density of the cooling water. T_{outlet} and T_{inlet} are the temperatures measured at the outlet and inlet of cooling water. Δt represents the cooling time, the time for the temperature difference $\Delta T = T_{outlet}(t) - T_{inlet}(t)$ to increase from zero to the maximum value and then decrease to zero. The schematic diagram of the calorimetric diagnostics system is shown in figure 3.6.

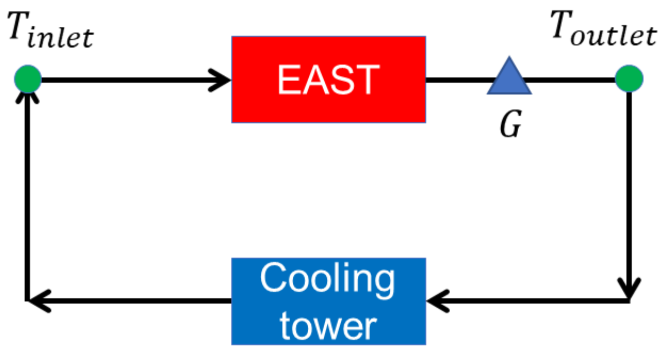

Figure 3.6. The schematic diagram of the calorimetric diagnostics system. The green circle and blue triangle represent the temperature sensors and flow meters of the water-cooling system, respectively.

The flow rate of cooling-water in each module is very stable during one campaign, and figure 3.7 shows the volume flow rate of cooling water in module A on April 8, 2023, throughout the day. Figure 3.8 (a) shows the outlet and inlet temperature of cooling water in module A for the whole day on April 8, 2023, and the temporal evolution of temperature difference for EAST discharge #122 058 is shown in (b). The duration of this discharge is 262.56 s with ~0.5 MW LHW 1, ~1.6 MW LHW 2, and ~1.7 MW ECRH. In Figure 3.8 (a), the significant fluctuations of water temperature observed between 0:00 and 12:00 are attributed to diurnal temperature variations, while the peaks in the water temperature curve between 12:00 and 24:00 are caused by the injection of energy during discharges.

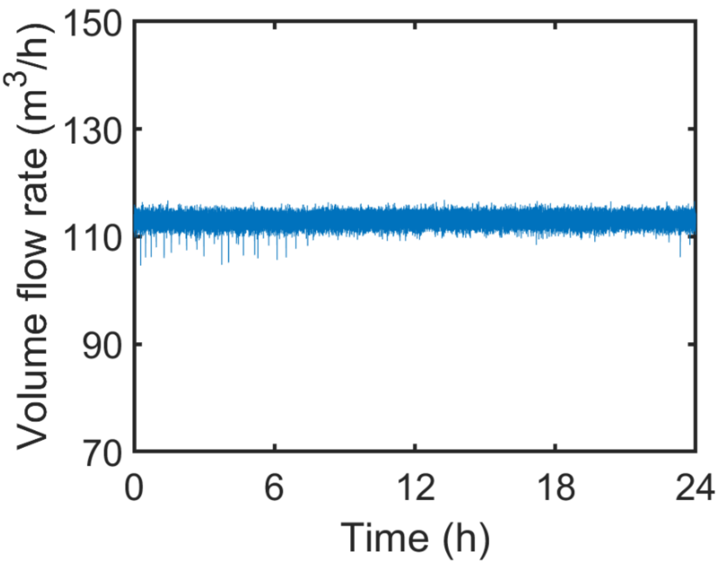

Figure 3.7. The volume flow rate of cooling water in module A.

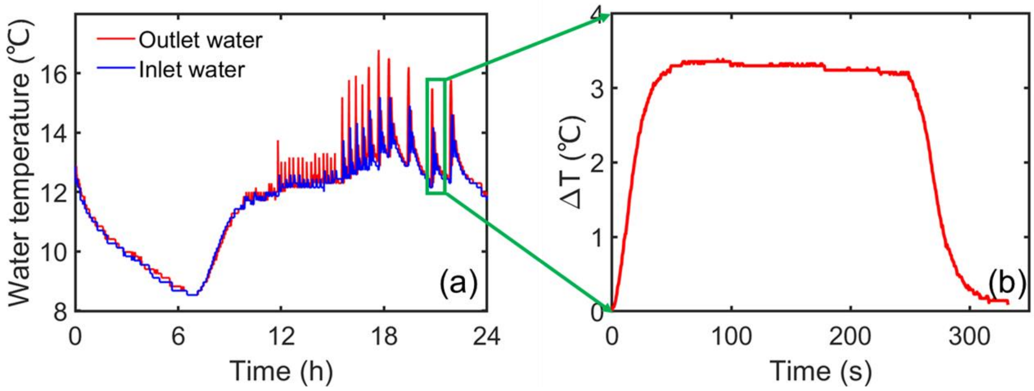

Figure 3.8. (a) The outlet and inlet temperature of cooling water in module A. (b) The temporal evolution of temperature difference for EAST discharge #122 058.

In figure 3.8 (a), the temperature increase of the inlet water is caused by the fact that the outlet water is not sufficiently cooled after passing through the cooling tower, then flow back to the inlet channel. This portion of water with temperature increments passes through the tokamak and then flow to the outlet channel and be measured, cause the further temperature increase of the outlet water. In addition, it takes some time for the cooling water to flow from the inlet to the outlet. When analyzing data from the calorimetric diagnostics system, this time delay between the inlet and outlet water temperature measurement should be taken into consideration, to eliminate the effect of insufficient cooling of the cooling water. The value of time delay can be determined by comparing the moments when the inlet and outlet water temperature data start to rise during the discharge. The effect of time delay and insufficient cooling have been eliminated in figure 3.8 (b)

The time delay and insufficient cooling of the cooling water have resulted in difficulties in data analysis of calorimetric diagnostics system during long-pulse discharges, while this difficulty does not exist in relatively short-pulse discharges.

3.3.2 Analysis of the cooling capacity of main PFCs in EAST through the calorimetric measurement

The data from the calorimetric system can be utilized to analyze the cooling capacity of the PFCs. The water-cooling curve of one module during discharge is the temporal evolution of the cooling power of the cooling water P_{cool}. P_{cool} can be calculated by

$$P_{cool} = CG\rho\Delta T \tag{3.5}$$

There are three typical water-cooling curves as shown in figure 3.9, and the definitions of t_1, t_2, t_3, and t_4 in figure 3.9 are shown in table 3.1.

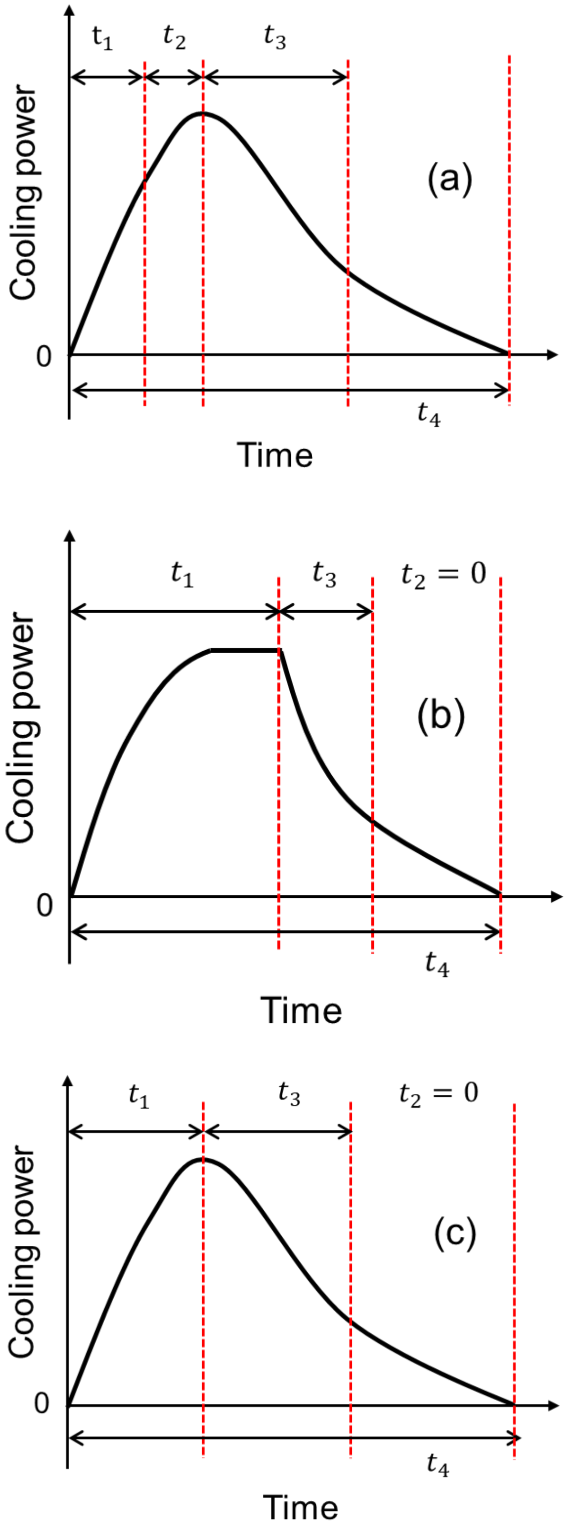

Figure 3.9. The three typical water-cooling curves.

Table 3.1. The definitions of t_1, t_2, t_3, and t_4.

t_1	The duration from the beginning to the end of the discharge.
t_2	The duration from the end of the discharge to reaching the maximum of ΔT.
t_3	Constant of water-cooling time, the duration from the maximum of ΔT $(\max \Delta T)$ to the $(\max \Delta T)/e$.
t_4	Cooling time, the duration from $\Delta T = 0$ to $\Delta T = 0$.

There are several indicators in the water-cooling curve that can be applied to evaluate the cooling performance of the module: (1) A shorter duration from $\Delta T = 0$ to $\max \Delta T$ in the water-cooling curve indicates a faster rising rate of the water-cooling curve, which implies better water-cooling capability. (2) A shorter t_2 indicates better water-cooling capability. In the case of figure 3.9(a), where $t_2 > 0$, the cooling power exhibits a further increase after the discharge termination, indicating a sustained rise in the temperature of the cooling water. This observation suggests the presence of heat accumulation within the module, which implies poor cooling performance of the module. In the case of figure 3.9(b) and (c), $t_2 = 0$, which exhibits better water-cooling capability. (3) A shorter t_3 indicates a faster cooling rate of the water-cooling system, which means a better water-cooling capability.

In addition, the flat-top phase in the curve of figure 3.9(b) indicates the achievement of power balance, where the energy load deposition on the module is the same as the energy carried away by the cooling water.

Figure 3.10 demonstrates the water-cooling curves of the upper divertor [figure (a)], lower divertor [figure (b)], and the first wall [figure (c)] for I-mode discharge #106 914 and H-mode discharge #110 726 (both performed after the upgrading of the lower diverter) in EAST, with the corresponding t_3 listed in table 3.2. The durations of discharges #106 914 and #110 726 were 124.65 and 225 s, respectively. Both discharges are double null configuration. The total injected energy in shots #106 914 and #110 726 were about 172.8 and 959.2 MJ, respectively. The curves in figure 3.10 indicate: (1) The lower divertor reached the power balance in both discharges. (2) All three modules exhibit good water-cooling capabilities, as indicated by $t_2 = 0$ in their respective water-cooling curves. (3) The lower divertor has better cooling ability, as it has shorter t_3 and faster rising rate of the water-cooling curve.

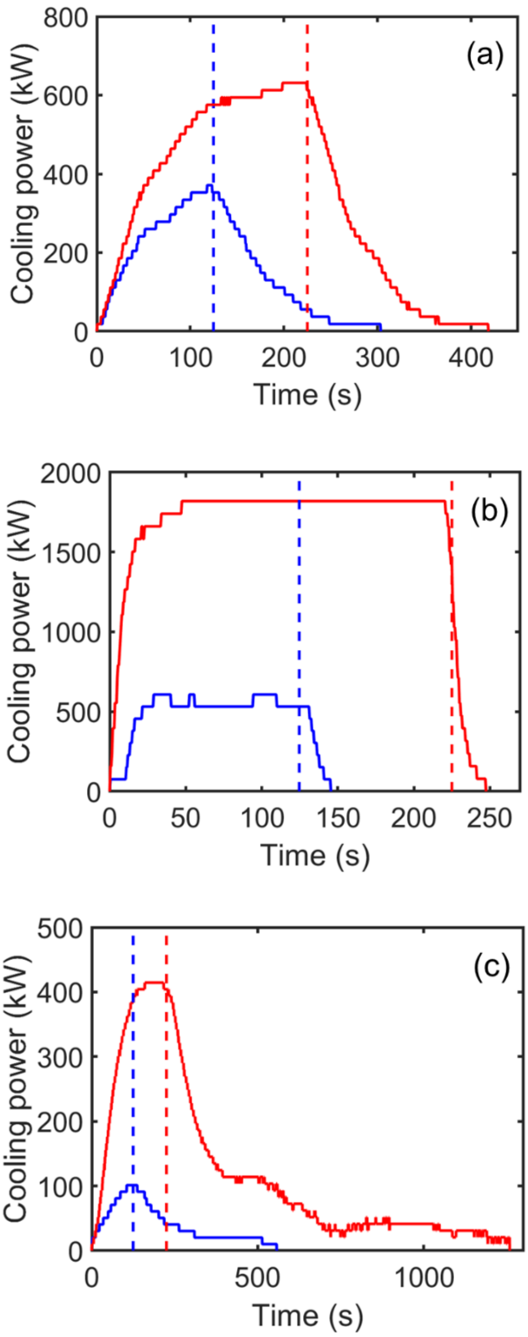

Figure 3.10. The water-cooling curves of the upper divertor (a), lower divertor (b), and the first wall (c) for I-mode discharge #106 914 (blue curve) and H-mode discharge #110 726 (red curve), where the solid line represents the water-cooling curve, and the dashed line indicates the moment of discharge termination.

Table 3.2. Constant of water-cooling time for the upper divertor, lower divertor, and the first wall for I-mode discharge #106 914 and H-mode discharge #110 726, unit s.

Discharge	Upper divertor	Lower divertor	The first wall
#106 914	56.8	6.7	125.7
#110 726	57.2	9.1	135.6

CHAPTER 4. Hot spot formation in the upper single null (USN) configuration discharges on the lower divertor

4.1 Experiment description

In the 2017 campaign of EAST, notable achievements were made in the attainment of high-performance long-pulse H-mode plasmas [118]. However, a tricky issue of undesired hot spots in the lower divertor region was observed. Prior to the steady-state 101.2 s H-mode shot #73 999, a series of shots were carried out to determine the optimal experiment conditions. These attempts included shots #73 991 to #73 998, excluding discharge #73 996 due to an unexpected termination of plasma occurring around 3.7 s.

Each of the seven discharges, was sustained for approximately 9.6 s. With direction of ion $B \times \nabla B$ drift pointed to the lower X-point, these discharges exhibited nearly identical physical parameters, as illustrated in figure 4.1 (with #73 993 and #73 994 as specific examples). For these shots, the plasma current was approximately 400 kA (figure 4.1(a)), while the loop voltage is controlled well, close to 0 V (figure 4.1(b)). This signifies that the majority of the plasma current was driven noninductively. The chord-averaged electron density at 6 s was approximately equal to $3.0 \times 10^{19}\ \mathrm{m}^{-3}$ (figure 4.1(c)), measured by the POlarimeter-INTerferometer diagnostics system (POINT) [119] at the middle plane. Power injection through the different auxiliary heating systems was of the following values: the power from the LHW 1 is approximately 0.43 MW, the power from the LHW 2 is approximately 1.48 MW, the power from the ECRH is approximately 0.35 MW, the power from the ICRF is approximately 0.12 MW (figure 4.1(d)). All auxiliary heating power with consistent magnitude and duration are injected into the seven shots, apart from shot #73 998, where the heating power of LHW 2 was approximately 10 kW greater than the other six shots. At 6 s, the stored energy was estimated to be approximately 1.30×10^{5} J (figure 4.1(e)).

Visible-light camera observations revealed the presence of hot spots in the lower divertor of port C at the same location in discharges #73 991, #73 992, and #73 993. However, in the case of discharges #73 994, #73 995, #73 997, and #73 998, hot spots did not manifest at the same location, as depicted in figure 4.2 (with #73 993 and #73 994 as specific examples). The total energy injection in shot #73 993 was approximately 16.06 MJ, with contributions from Ohmic heating (~0.34 MJ), LHW 1 (~3.10 MJ), LHW 2 (~9.42 MJ), ECRH (~2.47 MJ), and ICRF (~0.73 MJ). Similarly, in shot #73 994, the total energy injection was approximately 16.20 MJ, with contributions from Ohmic heating (~0.35 MJ), LHW 1 (~3.16 MJ), LHW 2 (~9.49 MJ), ECRH (~2.47 MJ), and ICRF (~0.73 MJ).

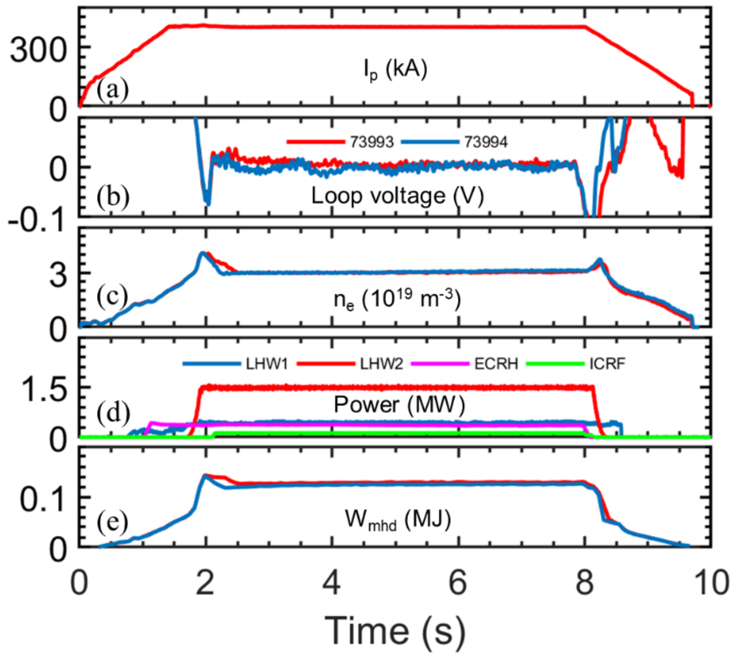

Figure 4.1. A comparison of various parameters between discharges #73 993 and #73 994 is presented. These parameters include: (a) plasma current, (b) loop voltage, (c) line-averaged electron density measured using the 6th chord of the POlarimeter-INTerferometer diagnostics system, (d) auxiliary heating power consists of the LHW system, ECRH system, and ICRF system (with all auxiliary heating power being the same for both discharges), and (e) stored energy [35].

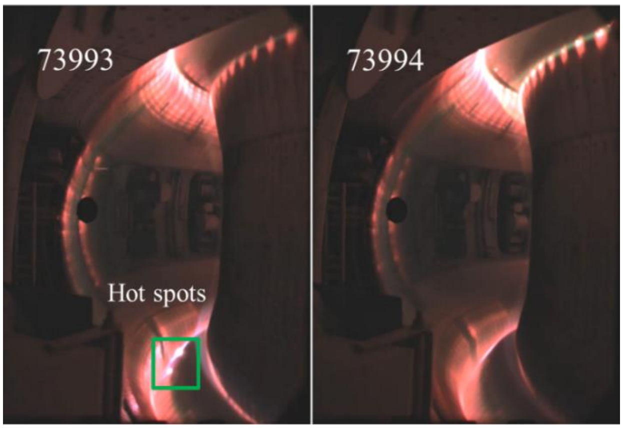

Figure 4.2. Pictures captured using a visible-light camera for discharges #73 993 and #73 994 at 6 s [35].

4.2 Heat load distribution in discharges with and without hot spot

The utilization of calorimetric system enables the investigation of the relationship between the formation of hot spots and the distribution of energy load on the plasma facing components. Table 4.1 presents the heat load removed by the cooling water flowing through modules A and E for shots #73 993 (hot spot appeared) and #73 994 (no hot spot appeared). The measured data indicate that the heat load removed by module E in shot #73 993 was larger in comparison to shot #73 994. Furthermore, the energy removed by module A in shot #73 993 was lower in comparison to shot #73 994. For shot #73 994, ratios of the energy removal from modules A and E to the overall injected power were calculated to be approximately 52.8% and 10.7%. These values are closely similar to mean rates of 47.1% and 11.5%, derived from a dataset encompassing numerous statistics for typical shots with upper single null configuration in the EAST 2017 campaign [59]. These findings provide evidence that, the hot spot appearance accompanied by a notable alteration in the distribution of energy load among different plasma facing materials.

The data obtained from calorimetric diagnostics system offers the opportunity to evaluate the extra energy load on the lower divertor. In the case of shot #73 993, the occurrence of hot spots was observed within a duration of approximately 3 to 8 s. A comparison of calorimetric measurements between shots #73 993 and #73 994 indicated a notable energy difference of 3.82 MJ within module E. Consequently, the additional deposited energy onto the lower divertor was estimated to be about 0.76 MW. Due to the limited field of view of the visible-light camera, it was not feasible to determine the total number of hot spots on the entire lower divertor, nor was it possible to estimate the energy flux on each individual hot spot. Nevertheless, the presence of hot spots has the potential to induce localized excessive heat flux, which significantly impacts the distribution of energy load on different plasma facing components.

Table 4.1. The energies removed by the cooling water in modules A and E for shots #73 993 and #73 994 were determined using the calorimetric diagnostics. The values enclosed in brackets represent the ratios of energies removed from each module with respect to the total power injection [35].

Discharge	Module A	Module E
#73 993	5.20 MJ (32.4%)	5.56 MJ (34.6%)
#73 994	8.56 MJ (52.8%)	1.74 MJ (10.7%)

4.3 Main parameters for hot spot formation

The magnetic topology from shot #73 991 to #73 998 (excluding #73 996) is the typical upper single null configuration in EAST. By comparing the plasma configuration of shot #73 993 (with hot spot) depicted in figure 1.4 and the hot spot position illustrated in figure 4.2, it was noticed that the hot spot position was in close proximity to the strike point (SP) on the lower outer target plate. Consequently, further investigation into the association between hot spot generation and the SP location becomes imperative in order to gain a reasonable interpretation of this phenomenon.

The stable plasma configurations for the seven analyzed shots were established starting from approximately 2.3 s which were determined using the EFIT code. Prior to this time, the configuration changes exhibited consistent trends among the seven shots. Hot spots appeared from around 3 s onwards. To investigate the time evolution of the SPs location on the lower outer divertor during the time interval from 3 to 8 s, the EFIT reconstruction was utilized. Figure 4.3 presents the calculated SPs location on the lower outer divertor for shots #73 991 to #73 998 (excluding #73 996). The red and blue points in figure 4.3 correspond to the heights of the SPs on the lower outer divertor for these 7 shots, with and without hot spots, in the cylindrical coordinate system. Remarkably, it was observed that the hot spot and lower outer SPs in all analyzed shots, within the time interval of 3 to 8 s, were situated on the lower divertor (outside dome). Figure 4.3 illustrates that the spatial separation between the hot spot and SP on the lower outer divertor did not exhibit a discernible correlation with hot spot formation across these shots. This observation arises from the fact that the location of the SP on the lower outer divertor for shots #73 994 and #73 995 (no hot spot appearance) was nearly identical to that of the shots with hot spots appearance.

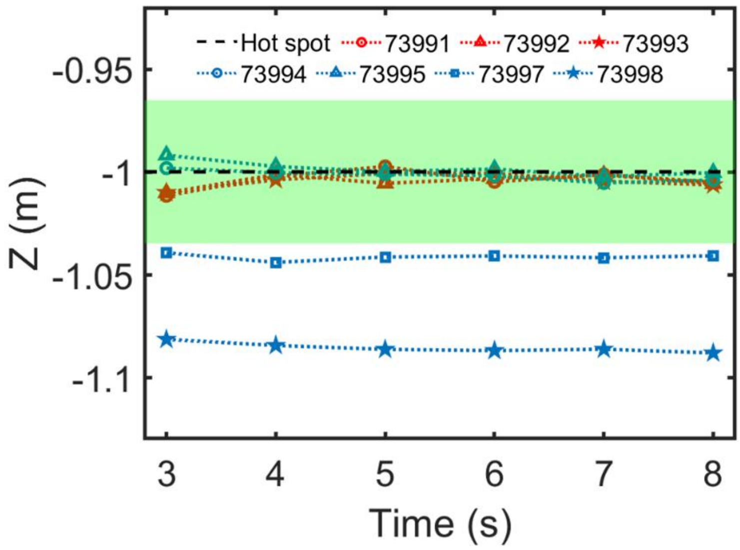

Figure 4.3. The temporal evolution of the height positions of the lower outer strike points of these seven shots in cylindrical coordinates was demonstrated. The shots with hot spots are represented by red lines, while the shots without hot spots are represented by blue lines. The height position of the hot spot on the lower dome is indicated by a black dashed line. Additionally, the estimated hot spot area is denoted by the green color [35].

The time evolution of the values of the $gapout$, dR_{sep}, and dR_{mid} were demonstrated from shot #73 991 to #73 998 (excluding #73 996), as depicted in figure

4.4. In Figure 4.4(a), the $gapout$ alone did not distinguish between shots with or without hot spot occurrences. However, shots with hot spots could be discerned based on the dR_{sep} and dR_{mid} values displayed in figures 4.4(b) and 4.4(c). Specifically, hot spots emerged in shots characterized by smaller dR_{sep} value and larger dR_{mid} value. EAST possesses the capability to finely manipulate the plasma magnetic topology by modifying the $gapout$ and dR_{sep} magnitudes at millimeter accuracy. Consequently, the distinction in the value of dR_{mid} between shots with and without hot spots, as depicted in figure 4.4(c), is not so evident as that of dR_{sep} in figure 4.4(b). Additionally, dR_{mid} can be indirectly controlled by adjusting the values of dR_{sep} and $gapout$. It is worth noting that the accumulation of zero drift in the magnetic measurement system can lead to distortion of the plasma configuration control in long pulse discharge. However, this issue has been resolved in 2019 campaign and explained in the next section.

Figure 4.4 provides a plausible correlation between the formation of hot spots and the plasma configuration in the plasma region outside the LCFS.

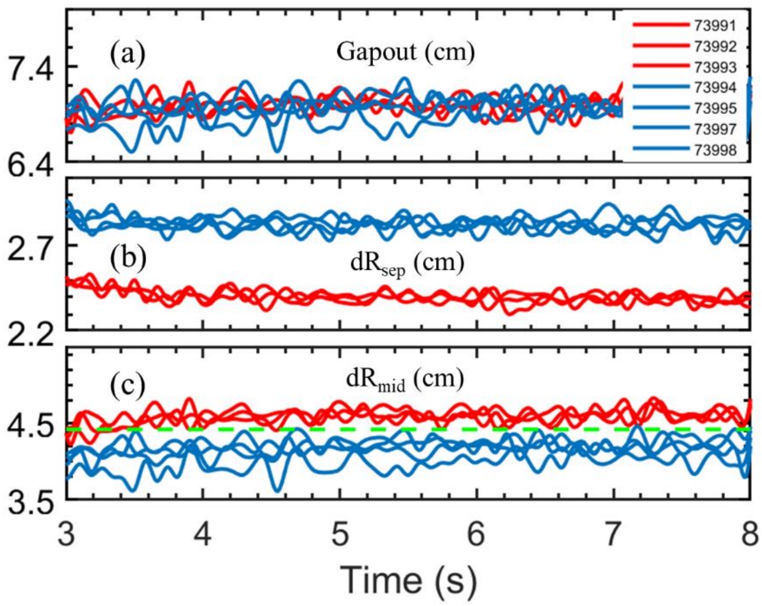

Figure 4.4. The temporal evolution of the values of $gapout$, dR_{sep}, and dR_{mid} for the seven shots is depicted, where shots with hot spots denoted by red lines and shots without hot spots denoted by blue lines [35].

The mechanism underlying the generation of hot spots in the above experiments was investigated through MFL tracking in the plasma region outside the LCFS utilizing the RGCO. Magnetic field line simulation was adopted because: (1) the orbit simulation of bulk electrons needs to consider Coulomb collisions, which are not included in RGCO, (2) the fast electrons in EAST are of keV magnitude and their orbit are along MFLs, (3) the energy transport in the SOL is along MFLs. Figure 4.5 demonstrates the simulation results, and the equilibrium magnetic configuration of shot #73 993 at 6 s were obtained from the EFIT reconstruction. As shown in figure 4.5, the motion of electrons along the red MFLs, associated with the dR_{mid} region, resulted in their hitting on the lower divertor, and ultimately leading to the generation of hot spots.

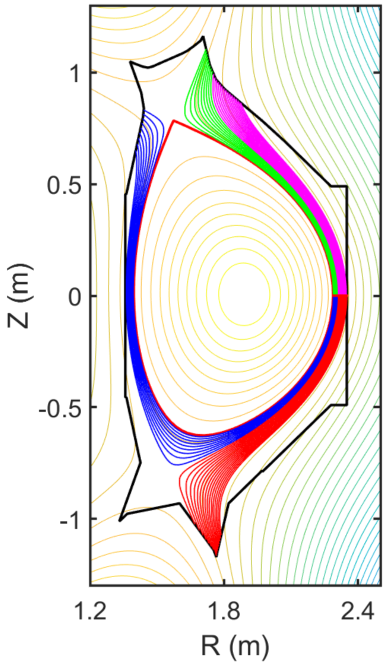

Figure 4.5. Magnetic field line tracking was conducted in the SOL to investigate the electron motion. The tracking analysis involved different sets of magnetic field lines, each representing distinct tracking directions and regions within the SOL. The blue magnetic field lines correspond to the forward electron tracking, and the onsets are in the dR_{sep} region, which is located between the primary and secondary separatrices. The red magnetic field lines correspond to the forward electron tracking, and the onsets are in the dR_{mid} region, which is located between the secondary separatrix and the first wall. The pink magnetic field lines correspond to the backward electron tracking, and the onsets are in the dR_{mid} region, which is located between the secondary

separatrix and the first wall. The green magnetic field lines correspond to the backward electron tracking, and the onsets are in the dR_{sep} region, which is located between the primary and secondary separatrices [35].

Magnetic field lines backward tracking originating from the hot spot region of shot #73 993 was conducted, as depicted in figure 4.6. The simulation was configured to auto-terminate when the tracked MFL reached the vicinity of the LHW antenna within the plasma region outside the LCFS. The results presented in figure 4.6 illustrate that the backward-tracked MFL could reach to the dR_{mid} area and finally stopped in front of the antennas of lower hybrid wave 1 and 2. The ends of the MFLs are indicated by black points in figure 4.6(a), revealing a broad distribution in both poloidal and toroidal directions in front of the lower hybrid wave antenna. These findings suggest that electrons in a large geometric space ahead of the lower hybrid wave antenna may absorb the energy from lower hybrid wave. Subsequently, these heated electrons hit the lower divertor region, thus contributing to the generation of hot spots.

The separation between the start points of the red and blue tracked MFLs in figure 4.6(b) was only approximately 6 mm within the hot spot region, however, notable differences in their trajectories is exhibited. As illustrated in figure 4.2, the observed hot spots in these shots exhibited a toroidal localization pattern. This phenomenon can be explained by the presence of small bulges on certain lower divertor materials, which create an enlarged contact area with the magnetic field lines. Consequently, a greater number of electrons can move along the MFLs and hit these specific bulges, leading to localized excessive energy loads on these regions.

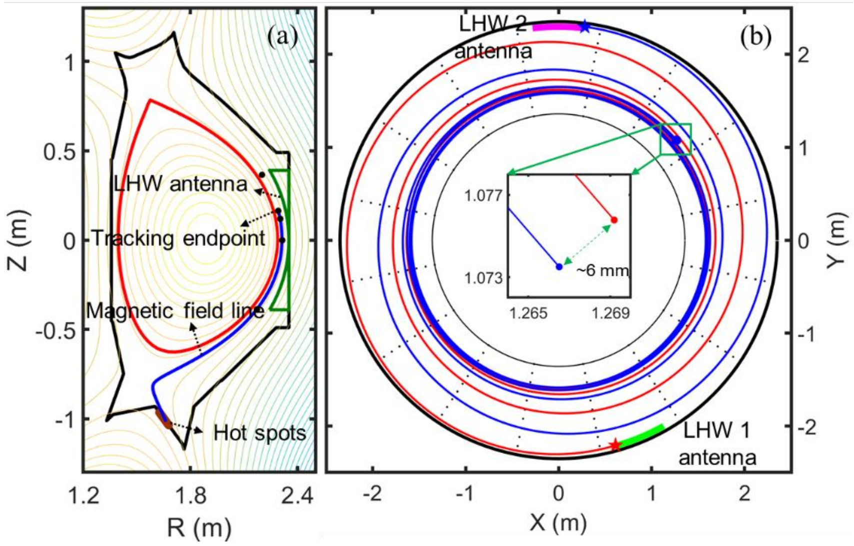

Figure 4.6. Demonstration of the magnetic field lines backward tracking in $R-Z$ view (a) and top view (b). In figure (b), the red and blue magnetic field lines can be back-tracked to the dR_{mid} region in front of the antenna for LHW 1 and 2, respectively. The color of the start and end points of each magnetic field line corresponds to the color of the line itself, with circles indicating the start points and stars representing the end points [35].

4.4 Appearance of hot spot in the 101.2 s H-mode discharge

From Sections 4.2 and 4.3, two conclusions can be drawn: (1) the emergence of hot spots is combined with a significant variation in the distribution of energy load among different plasma facing materials; and (2) large dR_{mid} tends to cause the hot spot generation on the lower divertor. These two findings can be proved in the later discharge #73 999.

As one of the contributions of this thesis, the SOL magnetic topology plays an essential role in the hot spot generation. This point has been delivered to EAST operators and used to mitigate the hot spot formation. EAST achieved the 101.2 s long-pulse H-mode shot #73 999. However, the magnetic measurement system of EAST existed an issue of zero drift, leading to minor but continuous modifications in the SOL magnetic configuration throughout the shot, as depicted in figure 4.7. Consequently, hot spots emerged on the lower divertor from approximately 55 s, and progressively intensifying over time, as illustrated in figure 4.8 captured by the visible-light camera.

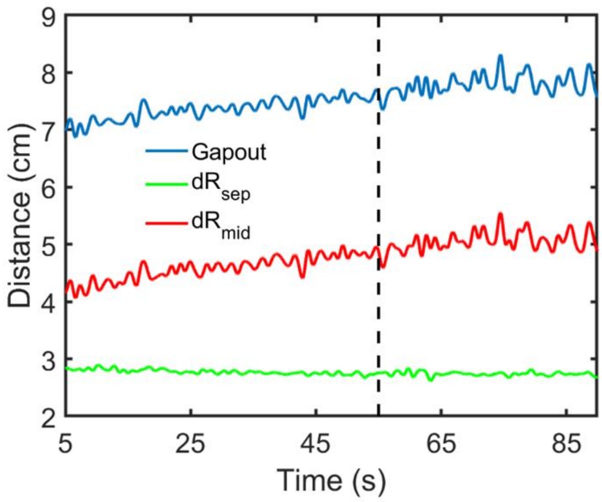

Figure 4.7. The time evolution of the value of $gapout$, dR_{sep}, and dR_{mid} for shot #73 999 [35].

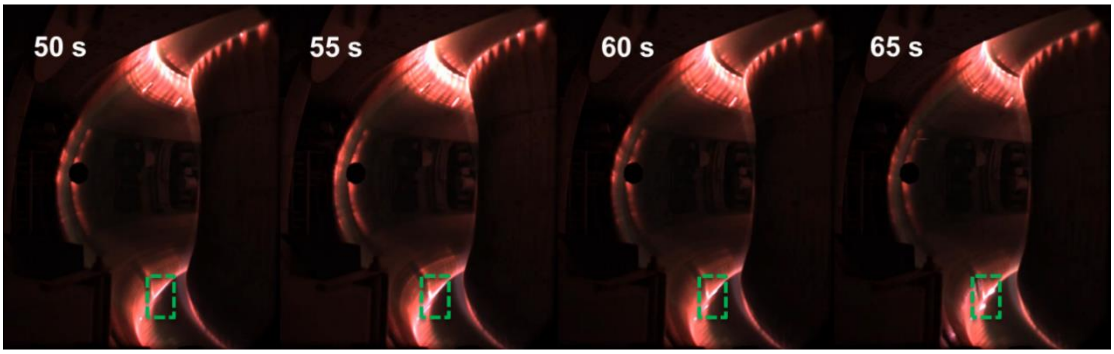

Figure 4.8. Visible-light camera images captured at 50 s, 55 s, 60 s, and 65 s for EAST shot #73 999 [35].

Figure 11(b) of the previous study [59] presented the observation of heat load redistribution among various PFCs following the formation of hot spots in EAST shot #73 999. The depicted red curve in the figure illustrates that, the energy removed from module A exhibited a decreasing trend starting at approximately 55 s. This decline implies a reduction of energy load on the upper divertor during this period, with a corresponding increase in power deposition on the lower divertor, as shown in the green curve.

The zero drift problem of the magnetic measurement system in EAST has been resolved by the application of a new designed analog integrator in the system [77, 120]. Benefiting from this upgrade, EAST can achieve more stable plasma configuration control in thousand-second discharge [121], and the hot spot formation has been mitigated.

CHAPTER 5. Hot spot formation in the LHW modulation experiment

5.1 Experimental results and heat load analysis

The analysis presented in Chapter 4 explains the generation of hot spots, which arise from the electrons in the plasma region outside the LCFS move along the MFLs and eventual hit the lower divertor components. Nonetheless, the precise energy source of electrons in the plasma region outside the LCFS is still unknown. Therefore, experimental shot #74 864 was conducted, involving LHW modulation at two frequencies.

The L-mode shot #74 864 followed a typical upper single null magnetic topology, where the direction of ion $B \times \nabla B$ drift pointed to the lower X-point. Figure 5.1 presents several significant plasma parameters for this shot. The plasma current reached approximately 400 kA (figure 5.1(a)). Throughout the flat-top phase, the electron density remained well-controlled, with a chord-averaged electron density in the middle plane around $\sim 2.23 \times 10^{19}\ \mathrm{m}^{-3}$ at 5 s (figure 5.1(c)). The power injection from the auxiliary heating systems consisted of two parts: approximately 0.52 MW from the 2.45 GHz LHW and approximately 0.58 MW from the 4.6 GHz LHW. The duty ratios for the 2.45 GHz and 4.6 GHz LHWs were approximately 50%, with each heating period lasting approximately 2 s (figure 5.1(d)). The phases of the injected lower hybrid waves at frequencies of 2.45 GHz and 4.6 GHz were 325° and 90°, and their power spectra were calculated through the ALOHA code [122], as depicted in figure 5.2. Notably, the plasma stored energy experienced a clear increase during the LHW injection, as demonstrated in figure 5.1(e). This observation suggests the effective plasma heating capability of the LHW. Moreover, the plasma loop voltage exhibited a decrease during the LHW injection, as shown in figure 5.1(b), indicating the sufficient drive of noninductive current in the core plasma through lower hybrid current driving. However, it is worth noting that the mean plasma loop voltage over the first 4.6 GHz lower hybrid wave injection was approximately 0.2 V, which was approximately 60 mV lower than that observed during the first 2.45 GHz lower hybrid wave injection. This disparity suggests distinct performance of the lower hybrid waves at frequencies of 2.45 GHz and 4.6 GHz during this discharge, with a higher efficiency of LHCD in the core plasma during the 4.6 GHz lower hybrid wave operation.

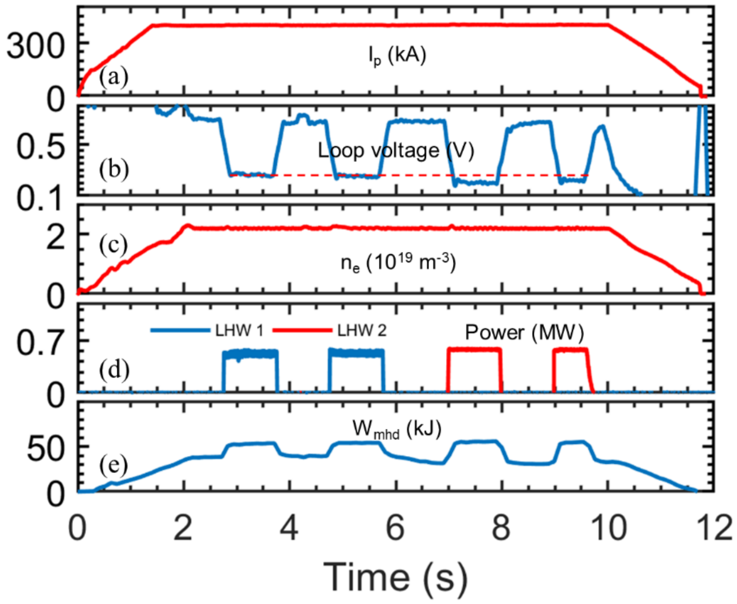

Figure 5.1. The plasma parameters of shot #74 864 were demonstrated. (a) the plasma current, (b) the loop voltage, (c) the line-averaged electron density measured through the POINT system, with measurement chord located in the middle plane, (d) the auxiliary heating power of LHW 1 (2.45 GHz) and LHW 2 (4.6 GHz), and (e) the stored energy [35].

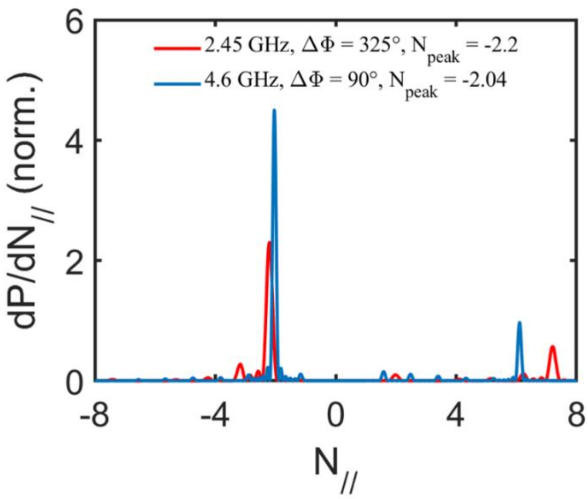

Figure 5.2. The normalized power spectra of the LHWs at 2.45 GHz and 4.6 GHz indicated in red and blue curve, respectively, calculated through the ALOHA code. Only demonstrate the spectra in the range of $-8 \le N_{\parallel} \le 8$ [35].

Figure 5.3(a) is a picture captured through the IR camera positioned in port G. On the left side of the figure, one can observe the LHW antenna operating at the frequency of 4.6 GHz, accompanied by two graphite guard limiters. To investigate the energy load deposited on the divertor components within the shot period, 4 representative patches were carefully selected as indicated in figure 5.3(a). Patches one and two, situated in the lower outer divertor, were chosen to compare the heat load in the presence and absence of hot spots, respectively. Patches three and four were situated in the outside and inside surfaces of the upper divertor. Particularly, the hot spot observed in patch one was potentially dangerous, while patch two served as a reference for comparison purposes. In this upper single null shot, it was anticipated that the upper divertor components would endure considerably greater energy loads than the lower divertor components, so patches three and four are selected in this research. Figure 5.3(b) portrays the average temperature variation of these four patches, measured by the IR camera. Figures 5.3(c) to 5.3(f) illustrate the temporal derivatives of temperature for the four selected patches. It is evident from figure 5.3(b) that the temperature in patch one exhibited a strong correlation with the injection of LHW at the frequency of 2.45 GHz. Nonetheless, following the second injection phase of 2.45 GHz LHW, the temperature in patch one displayed a continuous decrease, which weakly associated with the injection of 4.6 GHz LHW. This observation suggests that the formation of the hot spot in patch one is likely influenced by the different performance of these two frequencies of LHWs. Further investigation of this finding will be conducted in the subsequent section.

The temperatures in patches three and four changed simultaneously with the lower hybrid wave injection at frequencies of 2.45 GHz and 4.6 GHz. This synchronicity indicates that in this shot with USN configuration, the heat load deposited on the upper divertor comes from the plasma region inside the LCFS. Since the time derivative of temperature is strongly correlated with the energy flux, figures 5.3(e) and 5.3(f) demonstrate that the upper divertor component is subjected to a substantial energy flux during LHW operation. Furthermore, the position of patch one was subjected to a higher heat flux compared to patch two during LHW operation at 2.45 GHz, as depicted in figures 5.3(c) and 5.3(d).

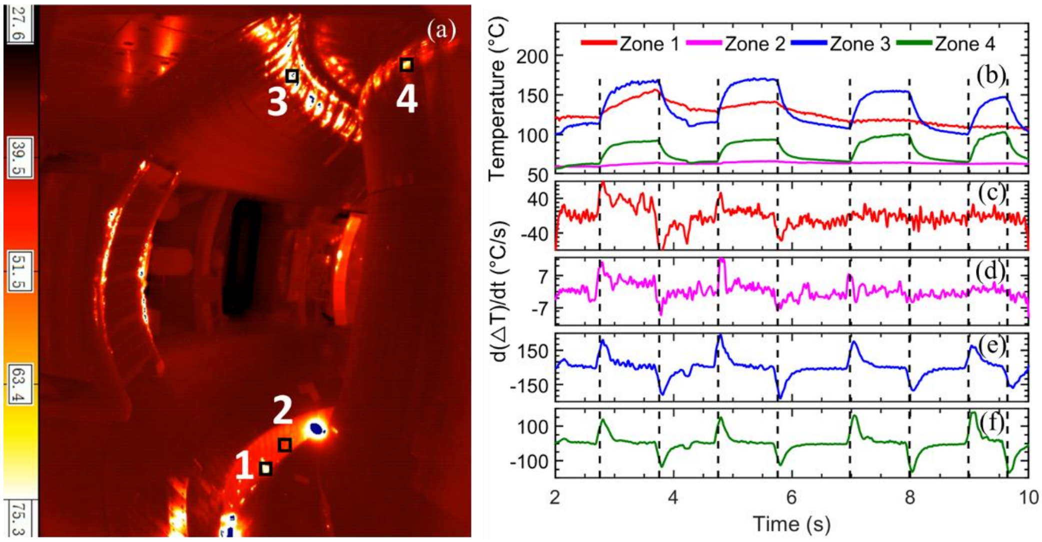

Figure 5.3. (a) Photograph captured by an IR camera for EAST shot #74 864. Patches one to four are clearly labeled in this photograph. (b) Temporal variation of the average temperature in the 4 patches labeled in figure 14(a). (c)–(f) Temporal derivatives of temperatures for the 4 patches [35].

5.2 Analysis of LHW power deposition

Extensive research conducted on various magnetic confinement devices have proved that LHW and LHCD are powerful approaches of electron heating and noninductive current driving, thereby facilitating steady-state and high-performance operation of the plasma [123]. The electrons received energy and momentum transferred from the lower hybrid wave mainly through the mechanism of electron Landau damping. In accordance with quasi-linear theory, electron Landau damping [124] occurs when the condition $\omega/k_{\parallel} \leq 3v_T$ is satisfied, in which $v_T = (2T_e/m_e)^{1/2}$. The corresponding equation can be expressed as below

$$N_{\parallel} \geq \frac{6.9}{\sqrt{T_e(keV)}} \tag{5.1}$$

Figure 5.2 displays the power density spectra of the LHW operating at frequencies of 2.45 and 4.6 GHz for the shot #74 864. Consequently, electron Landau damping occurs in the presence of quite high electron temperatures, typically in the range of several keV. However, when the electron temperature is relatively low, the lower hybrid wave can still transfer energy through the mechanism of collision damping. It is worth noting that the initial spectrum of the lower hybrid wave can be altered due to the parametric decay instability effect when lower hybrid waves cross the plasma region outside the LCFS before they reach the core plasma. For shot #74 864, the formation of hot spot on the lower divertor components was strongly associated with the 2.45 GHz LHW injection, and weakly associated with the 4.6 GHz LHW injection. To study this phenomenon, it is reasonable to firstly consider the potential impact of the PDI effect. This investigation involves analyzing the frequency spectrum broadening of the two lower hybrid waves, which can be determined using a radio frequency probe system mounted outside the first wall of the device. The position of the probe away from the LH antenna, ensured that the detected data was the result after the interaction of lower hybrid waves and plasma, rather than a direct measurement from the LH antenna. Figure 5.4 provides a comparison of the measured frequency spectra broadening for the 2.45 GHz LHW (red curve) and the 4.6 GHz LHW (blue curve). The spectrum widths of the two LHWs were found to be nearly identical, indicating that the parametric decay instability effect is not the main reason for hot spot generation.

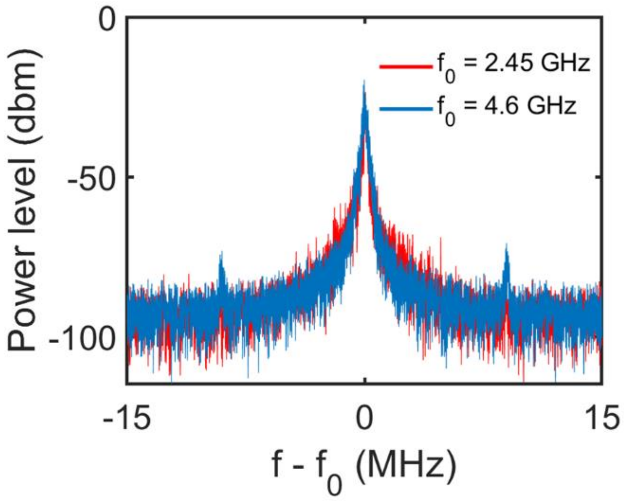

Figure 5.4. Frequency spectra broadening of the LHWs at frequencies of 2.45 GHz (represented by the red color) and 4.6 GHz (represented by the blue color) [35].

In accordance with the findings presented in Chapter 4, the hot spot formation on the lower divertor components is attributed to the motion of electrons follow the MFLs within the plasma region outside the LCFS starting from the front of the lower hybrid wave antenna. It is noteworthy that the electron temperature within the plasma region outside the LCFS remains quite low, necessitating consideration of the differential collision effects resulting from the injections of LHWs at frequencies of 2.45 and 4.6 GHz. The collision damping induced by the LHW [125] can be described by equation 5.2.

$$Im\ D^{(cl)} = \frac{\nu_{ei}}{\omega}\left(\frac{\omega_{pe}^2}{\omega_{ce}^2}N_\perp^2 + \frac{\omega_{pe}^2}{\omega^2}N_\parallel^2\right)N_\perp^2 \tag{5.2}$$

where $\nu_{ei} \propto n_e/T_e^{3/2}$ represents the electron–ion collision ratio, and $\omega = 2\pi f$ denotes the circular frequency of the LHW. Specifically, LHW 1 corresponds to the frequency of 2.45 GHz, while LHW 2 corresponds to the frequency of 4.6 GHz. In addition, $\omega_{ce} = eB/m_e$ signifies the electron cyclotron frequency, and $\omega_{pe} = (n_e e^2/m_e\varepsilon_0)^{1/2}$ represents the electron plasma frequency. Utilizing typical physics parameters of the EAST plasma outside the LCFS, where $n_e = 2.5 \times 10^{18}\ \mathrm{m}^{-3}$, allows us to calculate the approximate values of $\frac{\omega_{pe}^2}{\omega_{ce}^2} \approx 0.06$, $\frac{\omega_{pe}^2}{\omega^2} \approx 33.68$ (for LHW at 2.45 GHz), and $\frac{\omega_{pe}^2}{\omega^2} \approx 9.52$ (for LHW at 4.6 GHz). The magnitudes of $N_\parallel$ (near the main probe) and the correlative $N_\perp$ were of the same order. Consequently, in comparison to the second item, the first item in equation 5.2 is sufficiently minor and could be disregarded. Therefore,

$$Im\ D^{(cl)} \approx \frac{\nu_{ei}\omega_{pe}^2}{\omega^3} N_\parallel^2 N_\perp^2 \propto \frac{n_e^2}{T_e^{3/2}\omega^3} \tag{5.3}$$

As demonstrated by equation 5.3, the collision damping is significantly influenced by the LHW frequency. Assuming all other parameters remain constant, the collision effect induced by the lower hybrid wave operating at 2.45 GHz is approximately 6.6 times higher than that of the lower hybrid wave operating at 4.6 GHz. Collision damping mainly happens within the region of low electron temperatures, known as the SOL. Consequently, it can be inferred that, in comparison to the LHW at the frequency of 4.6 GHz, the 2.45 GHz LHW deposits more power into the plasma region outside the LCFS by collision process, consequently causing the hot spot formation on the lower divertor region. The localized generation of hot spot is likely attributed to minor bulges present in certain lower divertor tiles, as elaborated in Chapter 4. Moreover, in contrast to the LHW at frequency of 2.45 GHz, the 4.6 GHz LHW exhibits a greater energy deposition within the primary plasma region, which results in higher levels of LHCD and a lower loop voltage during the 4.6 GHz LHW injection, as mentioned in Section 5.1.

In order to obtain a more quantitative understanding of LHW energy deposition through different mechanisms at varying frequencies in this discharge, in comparison to the equation analysis, a simulation based on ray-tracing/Fokker–Planck model with GENRAY/CQL3D code package [126] [127] was performed, using 3.4 s and 7.4 s (2.45 GHz and 4.6 GHz lower hybrid wave operation) as examples.

In these two specified times, the electron densities were determined through a combination of the POINT diagnostics (measuring the core plasma) and the reflectometry (measuring the edge plasma), the electron temperatures were determined through a combination of the heterodyne radiometer (X-mode ECE) (measuring the core plasma) and the Thomson scattering system (measuring the main plasma). Additionally, the electron density and temperature values in the SOL were evaluated utilizing the equations provided in reference [128] as below.

$$n_e(\rho) = n_{e,LCFS} \exp\left(\frac{1-\rho}{\lambda_{ne}}\right) \tag{5.4}$$

$$T_e(\rho) = T_{e,LCFS} \exp\left(\frac{1-\rho}{\lambda_{te}}\right) \tag{5.5}$$

where λ_{ne} equals to 0.05 and λ_{te} equals to 0.02, adopting the empirical values of the EAST tokamak [129]. The simulation outcomes calculated by the GENRAY/CQL3D code are presented in table 5.1.

Table 5.1. The power absorption contributions attributed to electron Landau damping and collision damping for LHWs operating at frequencies of 2.45 GHz and 4.6 GHz [35].

Power absorption share	2.45 GHz LHW	4.6 GHz LHW
Electron Landau damping (kW)	396.6	463.7
Collision damping (kW)	141.3	106.1
Total power (kW)	537.9	569.8

Through the simulation, it is observed that the collision absorption power resulting from the injection of the 2.45 GHz LHW exceeded that of the 4.6 GHz LHW by about 35.2 kW. This finding aligns with the observed surface temperature evolution in patch one, as depicted in figure 5.3(b). It is worth noting that this difference of 35.2 kW is not as tremendous as the trend depicted in equation 5.3, which can be attributed to the presence of slight variations in the electron density and temperature profiles in the SOL when the two different frequencies of LHW injection.

This finding also confirms that, compared to 2.4 GHz LHW, 4.6 GHz LHW exhibits higher capabilities of electron heating and noninductive current driving in the core plasma, which has been employed to guide the EAST physics experiments.

CHAPTER 6. Summary and future work

6.1 Summary

The long-pulse steady-state plasma operation with high power injection is a key issue in magnetic confinement fusion research. In order to achieve higher plasma performance and confinement levels, various types of RF waves are often utilized for plasma auxiliary heating in experiments. However, due to engineering limitations and related physical issues, RF wave injection can sometimes cause excessive local heat loads on PFCs, leading to the hot spot formation as one of its manifestations. As a type of RF wave, LHW has been widely used in various devices due to its good plasma heating and current driving effects, and it is also an important means for EAST to achieve long-pulse steady-state operation. However, observations in EAST experiments have revealed that LHW injection leads to the generation of hot spots on the lower divertor. The formation of hot spots may result in melting of PFCs materials and impurity sputtering, and impurities entering the main plasma can degrade the plasma confinement, leading to a decrease in plasma quality or even plasma disruption. Therefore, measurement and study of the heat load on PFCs during discharges, investigation of the mechanisms of hot spot formation induced by RF wave injection, and research of the interaction between RF waves and plasma are crucial for the further enhancement of high-parameter, long-pulse operation capability of EAST, and even for the safe and steady-state operation of future fusion power plants. This thesis makes contributions to the field of fusion research in three fundamental areas, namely simulation, diagnostics, and physics experiment.

In terms of simulation:

It is a highly intuitive and effective approach to research the confinement and loss mechanisms of the charged particle through the combination of physics experiments and particle orbit simulation. In this study, a guiding center orbit tracking code incorporating relativistic effects was developed, which can be used for energetic particle orbit simulations in different devices. Compared to full orbit simulation model, guiding center orbit simulation model simplifies the Larmor gyration motion of the particle, resulting in a significant acceleration of particle orbit tracking, which facilitates particle orbit simulations under different conditions for detailed physics analysis. Based on this code, a study of energetic electrons in the QUEST device was conducted, providing physical pictures of the confinement of energetic electrons in the device.

In terms of diagnostics:

Calorimetric diagnostics system is one of the important heat load measurement systems in fusion devices, which indirectly measure the heat loads on PFCs by measuring the energy carried away by cooling water during discharges. In this study, the water-cooling capability of main PFCs in EAST was evaluated by the analysis of water-cooling curves, measured from the calorimetric diagnostics system. The results show that the water-cooling system of EAST can effectively cool the upper divertor, lower divertor and the first wall during discharges, ensuring the device safety. The excellent water-cooling capability can support longer pulse and higher power injection experiments on EAST. Additionally, the impact of hot spots formation on the energy load distribution among different plasma facing components was investigated using calorimetric diagnostics system. The results indicate that the presence of hot spots significantly alters the energy load distribution among different plasma facing components, with an increase of heat load on the plasma facing component where the hot spot is located and a decrease of heat load on other plasma facing components.

In terms of physics experiment:

The generation of hot spot on the lower divertor of EAST during discharges was observed using infrared and visible light cameras. The formation mechanism and energy source of hot spots have been clearly studied, which provides two primary insights. Firstly, minimize the deposition of auxiliary heating energy (such as LHW) within the plasma region outside the LCFS. This portion of power directly contributes to the energy load deposited on the plasma facing materials that are magnetically linked from the SOL. Consequently, endeavors should focus on enhancing the deposition of auxiliary heating energy within the main plasma for effective plasma heating and current driving. This approach will lead to improved plasma confinement and reduced cost-of-energy for the fusion device. Secondly. it is possible to redistribute the heat load among various PFCs by making slight modifications to the magnetic topology within the SOL. These findings provide a new solution for mitigating hot spots on PFCs during discharges, which is beneficial for achieving safe plasma operation of the device at longer pulse and higher parameters, and for accumulating valuable experience for the safe operation of future fusion power plants.

6.2 Future work

In this thesis, a preliminary study of the power balance topic in EAST and QUEST is presented, including the hot spot formation induced by LHW injection in EAST and the confinement of energetic electrons in QUEST. However, due to the broad range of research involved in power balance, there is still a need for further refinement in future research.

On the QUEST:

(1) A particle guiding center orbit tracking code that includes relativistic effects has been developed for studying the abundant energetic electrons observed in QUEST. The next step is to combine diagnostics data (such as hard X-rays and movable probes) from the experiment with the related electron orbit simulation results, to obtain the spatial and velocity-space distribution of energetic electrons in QUEST discharge. This will contribute to the research of the confinement and loss mechanisms of energetic electrons, also to the heat load distribution and mechanism of hot spot formation on QUEST.

(2) Produced from D-T nuclear fusion reaction, alpha particle plays an important role in the plasma self-heating in future fusion power plants, as shown in figure 6.1. This is a completely different heating source than the in-service tokamaks, and therefore difficult to study currently. With the similar physics properties, the behavior of alpha particle can be researched through energetic electron. Both energetic electron and alpha particle are energetic particles and therefore have similar collision situations. Alpha particle has positive charge and greater mass than energetic electron. The charge difference is not significant and the mass different play an essential role in the research. In QUEST, plenty of energetic electrons can be generated during ECW injection. Therefore, the study of confinement and loss mechanisms of alpha particle can be conducted through the related research of energetic electrons on QUEST.

(3) Perform the research of power balance on QUEST discharges, by utilizing calorimetric diagnostics system and other diagnostics measurements. The main energy loss channels of the future fusion power plants during operation are depicted in figure 6.1. For QUEST, physics processes related to alpha particle are missing because no D-T reaction occurs. The main energy loss channels of QUEST are outlined as follow: (a) particle and heat flux from the main plasma region, (b) particle and heat flux from the SOL region, (c) radiation, and (d) charge exchange (CX). Only by thoroughly studying the energy loss contributions from each channel during discharges can make sure the device safety during plasma experiments with longer pulse operation and higher power injection.

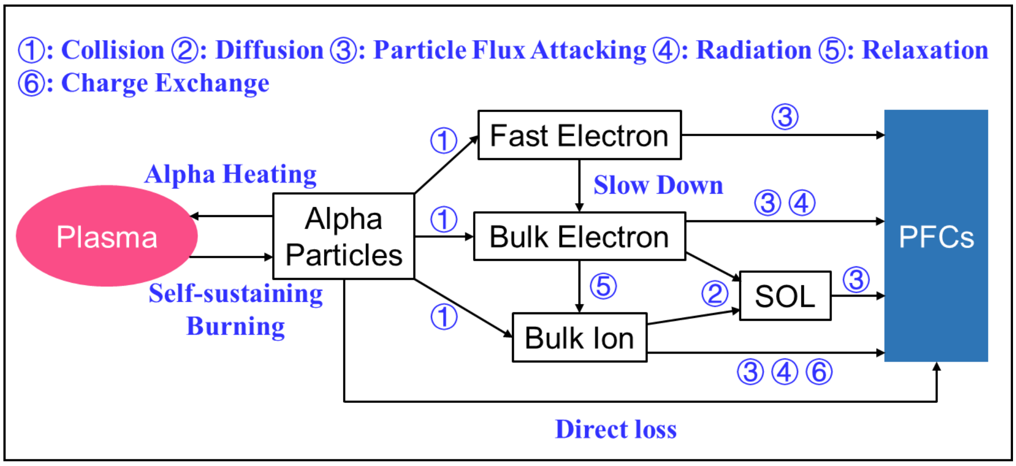

Figure 6.1. Diagram of energy transfer process in future fusion power plants.

On the EAST:

(1) Currently, calorimetric diagnostics system can achieve measurements of about 80% of the injection power during EAST discharge, with unaccounted heat loads potentially arising from the main limiter, RF antennas, guard limiters of the LHW and ICRF systems, as well as the ports not covered by the water-cooling system. In order to conduct power balance studies on EAST, achieving 100% measurement of the injection power is crucial. The next work is to expand the measurement range of the calorimetric diagnostics system to include the PFCs mentioned above. Subsequently, integrating with other diagnostics systems, such as infrared cameras and radiation diagnostics system, to achieve comprehensive measurement of power injection during discharges.

(2) Conducting research on the energy load distribution and power balance during long-duration high-parameter shots on EAST, and thoroughly clarifying the energy loss contributions from each channel. These results will be useful in predicting the core-to-edge energy flow in future fusion devises. All these researches can provide guidance for the safe operation of self-sustained future fusion power plants.

LIST OF PUBLICATIONS

Papers:

[1] **Wang Y**, Hanada K, Liu H, et al. Hot spots induced by RF-accelerated electrons in the scrape-off layer on Experimental Advanced Superconducting Tokamak[J]. Nuclear Fusion, 2023, 63: 056001.

[2] **Wang Y**, Hanada K, Sakurai D, et al. Phase jump detection and correction based on the support vector machine[J]. Plasma Physics and Controlled Fusion, 2023, 65: 065001.

[3] **Wang Y**, Hanada K, Hu Y, et al. Guiding center orbit simulation of energetic particles in tokamak plasma[J]. Proceedings of International Exchange and Innovation Conference on Engineering & Sciences, 2022, 8: 228-233.

[4] Li X, Wang S, ……, **Wang Y**, ……, et al. Local current shrinkage induced by the MARFE in L mode discharges on EAST tokamak[J]. AIP Advances, 2023, 13(3): 035037.

[5] Yuqi C, Haiqing L, ……, **Yunfei W**, ……, et al. Magnetohydrodynamic effect of internal transport barrier on EAST tokamak[J]. Plasma Science and Technology, 2022, 24(3): 035102.

[6] Xie J X, Wei X C, ……, **Wang Y F**, ……, et al. Development of a combined interferometer using millimeter wave solid state source and a far infrared laser on ENN's XuanLong-50 (EXL-50)[J]. Plasma Science and Technology, 2022, 24(6).

[7] Lan T, Liu H Q, ……, **Wang Y F**, ……, et al. Electron density profile reconstruction with convolutional neural networks[J]. Plasma Physics and Controlled Fusion, 2022, 64(12).

[8] Chu Y, Liu H, ……, **Wang Y**, ……, et al. Study of the mechanism of ITB formation and sustainment with optimized q profiles in ELMy H mode discharges on the EAST[J]. Plasma Physics and Controlled Fusion, 2021, 63(10): 105003.

Conferences:

[1] **Yunfei Wang**, Kazuaki Hanada, Haiqing Liu. Relativistic guiding center orbit simulation of fast electron loss in the EAST tokamak. European Conference on Plasma Diagnostics 2021, Jun. 7-11, 2021, Spain (online). Poster.

[2] **Yunfei Wang**, Kazuaki Hanada, Haiqing Liu, et al. Power balance investigation in long-pulse high-performance discharges in EAST tokamak. The 31st International Toki Conference on Plasma and Fusion Research, Nov. 8-11, 2022, Toki, Japan (online). Poster.

[3] **Yunfei Wang**, Kazuaki Hanada, Youjun Hu, et al. Guiding center orbit simulation of energetic particles in tokamak plasma. The 8th International

Exchange and Innovation Conference on Engineering & Sciences, Oct. 20-21, 2022, Fukuoka, Japan. Oral.

[4] **Yunfei Wang**, Kazuaki Hanada, Daisuke Sakurai, et al. Phase jump detection and correction based on the support vector machine. The 8th Conference on Fusion Plasma Diagnostics, Mar. 24-27, 2023, Zhuhai, China. Poster.

ACKNOWLEDGMENTS

Six years ago, as a master student of ASIPP (Institute of Plasma Physics, Chinese Academy of Sciences) and USTC (University of Science and Technology of China), I entered the field of magnetic confinement nuclear fusion and embarked on a challenging journey of exploration. Three years ago, I had the honor to pursue my doctor degree as an international student at Kyushu University in Japan. It was a great privilege that my master and doctor research were conducted on two world-renowned tokamaks, EAST and QUEST. During my doctoral stage, I have faced numerous challenges both academically and personally. I am grateful for the companionship and support I have received, as these have helped me to overcome challenges and gain valuable knowledge and life experience.

First and foremost, I would like to express my deepest gratitude to my supervisor, Professor Kazuaki Hanada. Hanada sensei is known for his rigorous academic attitude and fruitful research achievements. He has provided me with invaluable insights and suggestions for my research, which has greatly facilitated the progress of my work. I am highly appreciative of his patient guidance and revision of my papers, which have enabled successful publications and improved my scientific writing skills. He is approachable and has fostered a relaxed and pleasant atmosphere in our lab. With his care and assistance, I quickly adapted to my doctor research and life in Japan. Hanada sensei has served as a role model for me in both work and life.

My great gratitude also goes to Professors Haiqing Liu, Xiang Gao, and Yinxian Jie from ASIPP. With their selfless guidance and assistance, my academic research at EAST has progressed smoothly and achieved satisfied results. I also appreciate the EAST team, which is filled with passion and cohesion, and conducts outstanding physics experiments for me to learn from and research. The professors and students in the EAST team have provided me with valuable guidance and assistance.

I also wish to express my gratitude to Professor Hiroshi Idei, Professor Takeshi Ido, Associate Professor Ryuya Ikezoe, and Assistant Professor Takumi Onchi for their patient guidance and support, which has enabled me to quickly familiarize myself with the QUEST device and QUEST physics experiments, then perform research on QUEST. I would like to extend a special thanks to Assistant Professor Makoto Hasegawa for his selfless guidance in QUEST plasma equilibrium reconstruction.

My special thanks go to Professor Jinping Qian, Associate Professor Youjun Hu, as well as Assistant Professor Kaiyang He from ASIPP. It is their patient guidance that helped me quickly grasp the work of particle orbit simulation and develop the related program, which were initially unfamiliar to me.

I would like to express my gratitude to Associate Professor Daisuke Sakurai from Kyushu University and Associate Professor Ting Lan from ASIPP for their guidance and support in the field of machine learning.

I am grateful to the other professors and technicians of QUEST for their dedicated efforts, which have allowed for outstanding physics experiments on QUEST. I would like to express my appreciation to secretaries Yukie Urano, Sayuri Yoshinaga, Kazumi Ejima, Yuko Minamizato for their invaluable assistance in various aspects of my life.

My thanks are also expressed to classmate Qilin Yue, Yifan Zhang, Junyao Zhou, Yang Wang, Pakkapawn Prapan, Ryosuke Hiraka, Yuya Otsuka, and Yuji Koide for their tremendous support, which has helped me to quickly adapt to the QUEST experiments and life in Japan. I also extend my thanks to other students of QUEST for making my life rich and colorful.

Finally, I am deeply grateful to my parents for their selfless dedication, support, and encouragement at every step of my growth. Their unwavering support has allowed me to pursue my studies abroad with peace of mind.

REFERENCES

[1] Gandini A. From the Chicago Pile 1 to next-generation reactors[M]. Springer, 2004.

[2] Ichikawa H. Obninsk, 1955: The World's First Nuclear Power Plant and" The Atomic Diplomacy" by Soviet Scientists[J]. Historia Scientiarum. Second Series: International Journal of the History of Science Society of Japan, 2016, 26(1): 25-41.

[3] Dendy R O. Plasma physics: an introductory course[M]. Cambridge University Press, 1995.

[4] Betti R, Hurricane O A. Inertial-confinement fusion with lasers[J]. Nature Physics, 2016, 12(5): 435-448.

[5] Ongena J, Koch R, Wolf R, et al. Magnetic-confinement fusion[J]. Nature Physics, 2016, 12(5): 398-410.

[6] Di Nicola J-M G, Suratwala T, Pelz L, et al. Recent laser performance improvements and latest results at the National Ignition Facility[C]. //High Power Lasers for Fusion Research VII, 2023: PC1240103.

[7] Macisaac D. NIF Achieves Fusion Milestone[J]. The Physics Teacher, 2023, 61(2): 160-160.

[8] Post R F. The Magnetic-Mirror Approach to Fusion[J]. Nuclear Fusion, 1987, 27(10): 1579-1731.

[9] Burdakov A V, Ivanov A A, Kruglyakov E P. Modern magnetic mirrors and their fusion prospects[J]. Plasma Physics and Controlled Fusion, 2010, 52(12).

[10] Shafranov V D. Stellarators[J]. Nuclear Fusion, 1980, 20(9): 1075-1083.

[11] Nuhrenberg J, Zille R. Stable Stellarators with Medium-Beta and Aspect Ratio[J]. Physics Letters A, 1986, 114(3): 129-132.

[12] Boozer A H. What is a stellarator?[J]. Physics of Plasmas, 1998, 5(5): 1647-1655.

[13] Mukhovatov V, Shafranov V. Plasma equilibrium in a tokamak[J]. Nuclear Fusion, 1971, 11(6): 605.

[14] Artsimovich L. Tokamak devices[J]. Nuclear Fusion, 1972, 12(2): 215.

[15] Furth H. Tokamak research[J]. Nuclear Fusion, 1975, 15(3): 487.

[16] Porkolab M. Review of Rf Heating of Tokamaks[J]. Bulletin of the American Physical Society, 1977, 22(9): 1123-1123.

[17] Hwang D Q, Wilson J R. Radio-Frequency Wave Applications in Magnetic Fusion Devices[J]. Proceedings of the Ieee, 1981, 69(8): 1030-1043.

[18] Sweetman D R, Cordey J G, Green T S. Heating and Plasma Interactions with Beams of Energetic Neutral Atoms[J]. Philosophical Transactions of the Royal Society a-Mathematical Physical and Engineering Sciences, 1981, 300(1456): 589-598.

[19] Stork D. Neutral Beam Heating and Current Drive Systems[J]. Fusion Engineering and Design, 1991, 14(1-2): 111-133.

[20] Swanson D G. Radio-Frequency Heating in the Ion-Cyclotron Range of Frequencies[J]. Physics of Fluids, 1985, 28(9): 2645-2677.
[21] Bornatici M, Cano R, Debarbieri O, et al. Electron-Cyclotron Emission and Absorption in Fusion Plasmas[J]. Nuclear Fusion, 1983, 23(9): 1153-1257.
[22] Prater R. Recent Results on the Application of Electron-Cyclotron Heating to Tokamaks[J]. Journal of Fusion Energy, 1990, 9(1): 19-30.
[23] Golant V E. Plasma penetration near the lower hybrid frequency[J]. Soviet Physics Technical Physics, 1972, 16: 1980.
[24] Bonoli P. Linear theory of lower-hybrid wave in tokamak plasmas[J]. Wave heating and current drive in plasmas, 1985: 175-218.
[25] Orlinskij D V, Magyar G. Plasma Diagnostics on Large Tokamaks[J]. Nuclear Fusion, 1988, 28(4): 611-697.
[26] Hutchinson I H. Principles of plasma diagnostics[J]. Plasma Physics and Controlled Fusion, 2002, 44(12): 2603-2603.
[27] Xiao B J, Humphreys D A, Walker M L, et al. EAST plasma control system[J]. Fusion Engineering and Design, 2008, 83(2-3): 181-187.
[28] Wesson J, Campbell D J. Tokamaks[M]. 149. Oxford university press, 2011.
[29] Miyamoto K. Plasma physics for nuclear fusion[J], 1980.
[30] Wagner F, Becker G, Behringer K, et al. Regime of Improved Confinement and High-Beta in Neutral-Beam-Heated Divertor Discharges of the Asdex Tokamak[J]. Physical Review Letters, 1982, 49(19): 1408-1412.
[31] Stambaugh R D, Wolfe S M, Hawryluk R J, et al. Enhanced Confinement in Tokamaks[J]. Physics of Fluids B-Plasma Physics, 1990, 2(12): 2941-2960.
[32] Stangeby P C. The plasma boundary of magnetic fusion devices[M]. 224. Institute of Physics Pub. Philadelphia, Pennsylvania, 2000.
[33] Lipschultz B, Bonnin X, Counsell G, et al. Plasma–surface interaction, scrape-off layer and divertor physics: implications for ITER[J]. Nuclear Fusion, 2007, 47(9): 1189.
[34] Guo H, Li J, Gong X, et al. Approaches towards long-pulse divertor operations on EAST by active control of plasma–wall interactions[J]. Nuclear Fusion, 2013, 54(1): 013002.
[35] Wang Y, Hanada K, Liu H, et al. Hot spots induced by RF-accelerated electrons in the scrape-off layer on Experimental Advanced Superconducting Tokamak[J]. Nuclear Fusion, 2023, 63(5): 056001.
[36] Jacquet P, Colas L, Mayoral M L, et al. Heat loads on JET plasma facing components from ICRF and LH wave absorption in the SOL[J]. Nuclear Fusion, 2011, 51(10).
[37] Perkins F W. Radiofrequency Sheaths and Impurity Generation by Icrf Antennas[J]. Nuclear Fusion, 1989, 29(4): 583-592.
[38] Hanada K, Zushi H, Idei H, et al. Non-Inductive Start up of QUEST Plasma by RF Power[J]. Plasma Science & Technology, 2011, 13(3): 307-311.

[39] Gan K F, Li M H, Wang F M, et al. Hot spots generated by low hybrid wave absorption in the SOL on the EAST tokamak[J]. Journal of Nuclear Materials, 2013, 438: S364-S367.
[40] Perkins R J, Hosea J C, Kramer G J, et al. High-Harmonic Fast-Wave Power Flow along Magnetic Field Lines in the Scrape-Off Layer of NSTX[J]. Physical Review Letters, 2012, 109(4).
[41] Cesario R, Amicucci L, Cardinali A, et al. Current drive at plasma densities required for thermonuclear reactors[J]. Nature Communications, 2010, 1.
[42] Harris J H, Hutter T, Hogan J T, et al. Plasma-surface interactions with ICRF antennas and lower hybrid grills in Tore Supra[J]. Journal of Nuclear Materials, 1997, 241: 511-516.
[43] Mailloux J, Demers Y, Fuchs V, et al. Strong toroidal asymmetries in power deposition on divertor and first wall components during LHCD on TdeV and Tore Supra[J]. Journal of Nuclear Materials, 1997, 241: 745-749.
[44] Rantamaki K M, Petrzilka V, Andrew P, et al. Bright spots generated by lower hybrid waves on JET[J]. Plasma Physics and Controlled Fusion, 2005, 47(7): 1101-1108.
[45] Li Y L, Xu G S, Wu Z W, et al. Hot spots induced by LHCD in the shadow of antenna limiters in the EAST tokamak[J]. Physics of Plasmas, 2018, 25(8).
[46] Gunn J, Fuchs V, Petržílka V, et al. Measurement and modelling of suprathermal electron bursts generated in front of a lower hybrid antenna[J]. Nuclear Fusion, 2016, 56(3): 036004.
[47] Fuchs V, Goniche M, Demers Y, et al. Acceleration of electrons in the vicinity of a lower hybrid waveguide array[J]. Physics of Plasmas, 1996, 3(11): 4023-4035.
[48] Rantamaki K M, Pattikangas T J H, Karttunen S J, et al. Estimation of heat loads on the wall structures in parasitic absorption of lower hybrid power[J]. Nuclear Fusion, 2000, 40(8): 1477-1490.
[49] Barbato E. The role of non-resonant collision dissipation in lower hybrid current driven plasmas[J]. Nuclear Fusion, 2011, 51(10).
[50] Li M H, Ding B J, Liu F K, et al. Lower hybrid current drive experiments with different launched wave frequencies in the EAST tokamak[J]. Physics of Plasmas, 2016, 23(10).
[51] Cesario R, Cardinali A, Castaldo C, et al. Modeling of a lower-hybrid current drive by including spectral broadening induced by parametric instability in tokamak plasmas[J]. Physical Review Letters, 2004, 92(17).
[52] Wang L, Guo H Y, Ding F, et al. Advances in plasma-wall interaction control for H-mode operation over 100 s with ITER-like tungsten divertor on EAST[J]. Nuclear Fusion, 2019, 59(8).
[53] Litaudon X, Becoulet A, Crisanti F, et al. Progress towards steady-state operation and real-time control of internal transport barriers in JET[J]. Nuclear Fusion, 2003, 43(7): 565-572.

[54] Van Houtte D, Martin G, Becoulet A, et al. Recent fully non-inductive operation results in Tore Supra with 6 min, 1 GJ plasma discharges[J]. Nuclear Fusion, 2004, 44(5): L11-L15.

[55] Ide S, Team J-. Overview of JT-60U progress towards steady-state advanced tokamak[J]. Nuclear Fusion, 2005, 45(10): S48-S62.

[56] Zushi H, Nakamura K, Hanada K, et al. Steady-state tokamak operation, ITB transition and sustainment and ECCD experiments in TRIAM-1M[J]. Nuclear Fusion, 2005, 45(10): S142-S156.

[57] Park H K, Choi M J, Hong S H, et al. Overview of KSTAR research progress and future plans toward ITER and K-DEMO[J]. Nuclear Fusion, 2019, 59(11).

[58] Hanada K, Yoshida N, Honda T, et al. Investigation of hydrogen recycling in long-duration discharges and its modification with a hot wall in the spherical tokamak QUEST[J]. Nuclear Fusion, 2017, 57(12).

[59] Liu Y K, Gao X, Hanada K, et al. Power balance investigation in long-pulse high-performance discharges with ITER-like tungsten divertor on EAST[J]. Nuclear Fusion, 2020, 60(9).

[60] Ishiguro M, Hanada K, Liu H Q, et al. Direct measurement of energetic electron flow in Q-shu University experiment with steady-state spherical tokamak[J]. Review of Scientific Instruments, 2011, 82(11).

[61] Kojima S, Hanada K, Idei H, et al. Observation of second harmonic electron cyclotron resonance heating and current-drive transition during non-inductive plasma start-up experiment in QUEST[J]. Plasma Physics and Controlled Fusion, 2021, 63(10).

[62] Takase Y, Ejiri A, Fujita T, et al. Overview of spherical tokamak research in Japan[J]. Nuclear Fusion, 2017, 57(10).

[63] Hasegawa M, Nakamura K, Zushi H, et al. Development of a high-performance control system by decentralization with reflective memory on QUEST[J]. Fusion Engineering and Design, 2015, 96-97: 629-632.

[64] Hasegawa M, Nakamura K, Zushi H, et al. Current status and prospect of plasma control system for steady-state operation on QUEST[J]. Fusion Engineering and Design, 2016, 112: 699-702.

[65] Hanada K, Zushi H, Idei H, et al. Power balance estimation in long duration discharges on QUEST[J]. Plasma Science and Technology, 2016, 18(11): 1069.

[66] Wang Y, Hanada K, Hu Y, et al. Guiding center orbit simulation of energetic particles in tokamak plasma[J]. Proceedings of International Exchange and Innovation Conference on Engineering & Sciences, 2022, 8: 228-233.

[67] Dawson J M. Particle Simulation of Plasmas[J]. Reviews of Modern Physics, 1983, 55(2): 403-447.

[68] Pankin A, Mccune D, Andre R, et al. The tokamak Monte Carlo fast ion module NUBEAM in the National Transport Code Collaboration library[J]. Computer Physics Communications, 2004, 159(3): 157-184.

[69] White R T, Chance M. Hamiltonian guiding center drift orbit calculation for plasmas of arbitrary cross section[J]. The Physics of fluids, 1984, 27(10): 2455-2467.

[70] Hirvijoki E, Asunta O, Koskela T, et al. ASCOT: Solving the kinetic equation of minority particle species in tokamak plasmas[J]. Computer Physics Communications, 2014, 185(4): 1310-1321.
[71] Bittencourt J A. Fundamentals of plasma physics[M]. Springer Science & Business Media, 2004.
[72] Chen F F. Introduction to plasma physics[M]. Springer Science & Business Media, 2012.
[73] Goldston R J. Introduction to plasma physics[M]. CRC Press, 2020.
[74] Montgomery D C, Tidman D A. Plasma kinetic theory[J]. McGraw-Hill Advanced Physics Monograph Series, 1964.
[75] Lao L L, Stjohn H, Stambaugh R D, et al. Reconstruction of Current Profile Parameters and Plasma Shapes in Tokamaks[J]. Nuclear Fusion, 1985, 25(11): 1611-1622.
[76] Lao L L, Ferron J R, Groebner R J, et al. Equilibrium-Analysis of Current Profiles in Tokamaks[J]. Nuclear Fusion, 1990, 30(6): 1035-1049.
[77] Liu D, Wang X, Shen B, et al. An analog-digital integrator for EAST long pulse discharge[J]. Fusion Engineering and design, 2021, 165: 112255.
[78] Stringer T E. Effect of Magnetic-Field Ripple on Diffusion in Tokamaks[J]. Nuclear Fusion, 1972, 12(6): 689-694.
[79] Wang F, Zhao R, Wang Z X, et al. PTC: Full and Drift Particle Orbit Tracing Code for alpha Particles in Tokamak Plasmas[J]. Chinese Physics Letters, 2021, 38(5).
[80] Cary J R, Brizard A J. Hamiltonian theory of guiding-center motion[J]. Reviews of modern physics, 2009, 81(2): 693.
[81] Dormand J R, Prince P J. A family of embedded Runge-Kutta formulae[J]. Journal of computational and applied mathematics, 1980, 6(1): 19-26.
[82] Butcher J C. A history of Runge-Kutta methods[J]. Applied numerical mathematics, 1996, 20(3): 247-260.
[83] Xu Y F, Li L, Hu Y J, et al. Numerical simulations of NBI fast ion loss with RMPs on the EAST tokamak[J]. Nuclear Fusion, 2020, 60(8).
[84] Wu S, Team E. An overview of the EAST project[J]. Fusion Engineering and Design, 2007, 82(5-14): 463-471.
[85] Song Y T, Wan B N, Gong X Z, et al. Recent EAST Experimental Results and Systems Upgrade in Support of Long-Pulse Steady-State Plasma Operation[J]. Ieee Transactions on Plasma Science, 2022, 50(11): 4330-4334.
[86] Aymar R, Barabaschi P, Shimomura Y. The ITER design[J]. Plasma Physics and Controlled Fusion, 2002, 44(5): 519.
[87] Holtkamp N, Team I P. An overview of the ITER project[J]. Fusion Engineering and Design, 2007, 82(5-14): 427-434.
[88] Ikeda K. Progress in the ITER physics basis[J]. Nuclear Fusion, 2007, 47(6): E01.
[89] Song Y T, Wu S T, Li J G, et al. Concept design of CFETR tokamak machine[J]. Ieee Transactions on Plasma Science, 2014, 42(3): 503-509.

[90] Wan Y, Li J, Liu Y, et al. Overview of the present progress and activities on the CFETR[J]. Nuclear Fusion, 2017, 57(10): 102009.
[91] Zhuang G, Li G, Li J, et al. Progress of the CFETR design[J]. Nuclear Fusion, 2019, 59(11): 112010.
[92] Xu G, Wang L, Yao D, et al. Physics design of new lower tungsten divertor for long-pulse high-power operations in EAST[J]. Nuclear Fusion, 2021, 61(12): 126070.
[93] Qian J P, Gong X Z, Wan B N, et al. Integrated Operating Scenario to Achieve 100-Second, High Electron Temperature Discharge on EAST[J]. Plasma Science & Technology, 2016, 18(5): 457-459.
[94] Gong X, Garofalo A M, Huang J, et al. Integrated operation of steady-state long-pulse H-mode in Experimental Advanced Superconducting Tokamak[J]. Nuclear Fusion, 2019, 59(8).
[95] Wang L, Guo H, Ding F, et al. Advances in plasma–wall interaction control for H-mode operation over 100 s with ITER-like tungsten divertor on EAST[J]. Nuclear Fusion, 2019, 59(8): 086036.
[96] Song Y T, Zou X L, Gong X Z, et al. Realization of thousand-second improved confinement plasma with Super I-mode in Tokamak EAST[J]. Science Advances, 2023, 9(1).
[97] Liu Y K, Hamada N, Hanada K, et al. Preliminary study on heat load using calorimetric measurement during long-pulse high-performance discharges on EAST[J]. Plasma Physics and Controlled Fusion, 2017, 59(4).
[98] Zhuang Q, Ming T F, Yu Y W, et al. Calorimetry system for heat load in long-pulse discharges on EAST tokamak[J]. Physica Scripta, 2022, 97(9).
[99] Chen M W, Yang X F, Gong X Z, et al. Integrated infrared and visible tangential wide-angle viewing systems for surface temperature measurement and discharge monitoring in EAST[J]. Fusion Engineering and Design, 2020, 150.
[100] Zhang J Y, Zhang B, Gong X, et al. Development of a new dynamic foveated imager on wide-angle infra-red thermography system to improve local spatial resolution in EAST[J]. Review of Scientific Instruments, 2020, 91(11).
[101] Xu J C, Wang L, Xu G S, et al. Upgrade of Langmuir probe diagnostic in ITER-like tungsten mono-block divertor on experimental advanced superconducting tokamak[J]. Review of Scientific Instruments, 2016, 87(8).
[102] Xu J C, Wang L, Xu G S, et al. Design of Langmuir probe diagnostic system for the upgraded lower tungsten divertor in EAST tokamak[J]. Review of Scientific Instruments, 2018, 89(10).
[103] Duan Y M, Hu L Q, Mao S T, et al. Measurement of Radiated Power Loss on EAST[J]. Plasma Science & Technology, 2011, 13(5): 546-549.
[104] Duan Y M, Hu L Q, Mao S T, et al. The resistive bolometer for radiated power measurement on EAST[J]. Review of Scientific Instruments, 2012, 83(9).
[105] Gaspar J, Gardarein J L, Rigollet F, et al. Nonlinear heat flux estimation in the JET divertor with the ITER like wall[J]. International Journal of Thermal Sciences, 2013, 72: 82-91.

[106] Gaspar J, Corre Y, Firdaouss M, et al. First heat flux estimation in the lower divertor of WEST with embedded thermal measurements[J]. Fusion Engineering and Design, 2019, 146: 757-760.
[107] Gao J M, Li W, Xia Z W, et al. Analysis of Divertor Heat Flux with Infrared Thermography During Gas Fuelling in the HL-2A Tokamak[J]. Plasma Science & Technology, 2013, 15(11): 1103-1107.
[108] Petrie T W, Hill D N, Baptista J, et al. Infrared Thermography System on Diii-D[J]. Review of Scientific Instruments, 1990, 61(11): 3557-3561.
[109] Chankin A V, Summers D D R, Jackel H J, et al. Infrared Measurements of the Divertor Power at Jet[J]. Plasma Physics and Controlled Fusion, 1994, 36(3): 403-415.
[110] Itami K, Shimada M, Hosogane N. Characteristics of Divertor Plasma and Scrape-Off Layer in Jt-60u[J]. Journal of Nuclear Materials, 1992, 196: 755-758.
[111] Kang C S, Lee H H, Oh S, et al. Study on the heat flux reconstruction with the infrared thermography for the divertor target plates in the KSTAR tokamak[J]. Review of Scientific Instruments, 2016, 87(8).
[112] Eich T, Kallenbach A, Pitts R A, et al. Divertor power deposition and target current asymmetries during type-1 ELMS in ASDEX Upgrade and JET[J]. Journal of Nuclear Materials, 2007, 363: 989-993.
[113] Brunner D, Labombard B, Payne J, et al. Comparison of heat flux measurements by IR thermography and probes in the Alcator C-Mod divertor[J]. Journal of Nuclear Materials, 2011, 415(1): S375-S378.
[114] Carpentier S, Corre Y, Chantant M, et al. Study of heat flux deposition on the limiter of the Tore Supra tokamak[J]. Journal of Nuclear Materials, 2009, 390-91: 955-958.
[115] Mastrovito D, Maingi R, Kugel H W, et al. Infrared camera diagnostic for heat flux measurements on the National Spherical Torus Experiment[J]. Review of Scientific Instruments, 2003, 74(12): 5090-5092.
[116] Gan K F, Ahn J W, Park J W, et al. 2D divertor heat flux distribution using a 3D heat conduction solver in National Spherical Torus Experiment[J]. Review of Scientific Instruments, 2013, 84(2).
[117] Halliday D, Resnick R, Walker J. Fundamentals of physics[M]. John Wiley & Sons, 2013.
[118] Wan B N, Liang Y, Gong X Z, et al. Recent advances in EAST physics experiments in support of steady-state operation for ITER and CFETR[J]. Nuclear Fusion, 2019, 59(11).
[119] Wang Y F, Liu H Q, Jie Y X, et al. Optimization of the POlarimeter-INTerferometer diagnostics system on EAST[J]. Journal of Instrumentation, 2020, 15(6).
[120] Wang Y, Wang F, Ji Z, et al. A New Analog Integrator for Magnetic Diagnostics on EAST[J]. IEEE Transactions on Nuclear Science, 2019, 66(7): 1335-1339.

[121] Song Y, Zou X, Gong X, et al. Realization of thousand-second improved confinement plasma with Super I-mode in Tokamak EAST[J]. Science Advances, 2023, 9(1): eabq5273.
[122] Hillairet J, Voyer D, Ekedahl A, et al. ALOHA: an Advanced LOwer Hybrid Antenna coupling code[J]. Nuclear Fusion, 2010, 50(12).
[123] Fisch N J. Confining a Tokamak Plasma with Rf-Driven Currents[J]. Physical Review Letters, 1978, 41(13): 873-876.
[124] Decker J, Peysson Y, Hillairet J, et al. Calculations of lower hybrid current drive in ITER[J]. Nuclear Fusion, 2011, 51(7).
[125] Bonoli P T, Englade R C. Simulation-Model for Lower Hybrid Current Drive[J]. Physics of Fluids, 1986, 29(9): 2937-2950.
[126] Smirnov A, Harvey R. Calculations of the current drive in DIII-D with the GENRAY ray tracing code[J]. Bull. Am. Phys. Soc, 1995, 40(1837): 35.
[127] Harvey R, Mccoy M. The cql3d fokker-planck code[C]. //Proceedings of the IAEA Technical Committee Meeting on Simulation and Modeling of Thermonuclear Plasmas, 1992: 489-526.
[128] Wallace G M, Parker R R, Bonoli P T, et al. Absorption of lower hybrid waves in the scrape off layer of a diverted tokamak[J]. Physics of Plasmas, 2010, 17(8).
[129] Wu C B, Ding B J, Li M H, et al. Modeling the spectral modification of lower hybrid wave in the presence of drift-wave type density fluctuation in the scrape-off-layer of the EAST tokamak[J]. Physics of Plasmas, 2021, 28(8).